ANALYSIS OF PRECIPITATION USING SATELLITE OBSERVATIONS AND COMPARISONS WITH GLOBAL CLIMATE MODELS

A Dissertation

by

ADITYA MURTHI

Submitted to the Office of Graduate Studies of
Texas A&M University
in partial fulfillment of the requirements for the degree of

DOCTOR OF PHILOSOPHY

May 2010

Major Subject: Atmospheric Sciences

ANALYSIS OF PRECIPITATION USING SATELLITE OBSERVATIONS AND COMPARISONS WITH GLOBAL CLIMATE MODELS

A Dissertation

by

ADITYA MURTHI

Submitted to the Office of Graduate Studies of
Texas A&M University
in partial fulfillment of the requirements for the degree of

DOCTOR OF PHILOSOPHY

Approved by:

Chair of Committee,	Kenneth P. Bowman
Committee Members,	Gerald R. North
	Ramalingam Saravanan
	Prabir Daripa
Head of Department,	Kenneth P. Bowman

May 2010

Major Subject: Atmospheric Sciences

ABSTRACT

Analysis of Precipitation Using Satellite Observations and Comparisons with Global Climate Models. (May 2010)

Aditya Murthi, B.E., Bharathiyar University;

M.S., Texas A&M University

Chair of Advisory Committee: Dr. Kenneth P. Bowman

In this study, the space-time relationship of precipitation fields is examined by testing the Taylor's "frozen field" hypothesis (TH). Specifically, the hypothesis supposes that if a spatio-temporal precipitation field with a stationary covariance $\mathrm{Cov}(\mathbf{r}, \tau)$ in both space $\mathbf{r}$ and time τ, moves with a constant velocity $\mathbf{v}$, then the temporal covariance at time lag τ is equal to the spatial covariance at space lag $\mathbf{v}\tau$, that is, $\mathrm{Cov}(\mathbf{0}, \tau) = \mathrm{Cov}(\mathbf{v}\tau, 0)$. Of specific interest is whether there is a cut-off or decorrelation time scale for which the TH holds for a given mean flow velocity $\mathbf{v}$. The validity of the TH is tested for precipitation fields using high-resolution gridded NEXRAD radar reflectivity data over southeastern United States by employing two different statistical approaches. The first method is based upon rigorous hypothesis testing while the second is based on a simple correlation analysis, which neglects possible dependencies in the correlation estimates. The data-set has an approximate horizontal resolution of 4 km x 4 km and a temporal resolution of 15 minutes, while the time period of study is 4 days. The results of both statistical methods suggest that the TH might hold for the shortest space and time scales resolved by the data (4 km and 15 minutes), but that it does not hold for longer periods or larger spatial scales.

The fidelity of global climate models in accurately simulating seasonal mean precipitation in the tropics is investigated by comparisons with satellite observa-

tions. Specifically, six-year long (2000-2005) simulations are performed using a high-resolution (36-km) Weather Research Forecast (WRF) model and the Community Atmosphere Model (CAM) at T85 spatial resolution and the results are compared with satellite observations from the Tropical Rainfall Measuring Mission (TRMM). The primary goal is to study the annual cycle of rainfall over four land regions of the tropics namely, the Indian monsoon, the Amazon, tropical Africa and the North American monsoon. The results indicate that the WRF model systematically underestimates the magnitude of monthly mean rainfall over most Tropical land regions but gets the seasonal timing right. On the other hand, CAM produces rainfall magnitudes that are closer to the observations but the rainfall peak leads or lags the observations by a month or two. Some of these regional biases can be attributed to erroneous circulation and moisture surpluses/deficits in the lower troposphere in both models. Overall, the results seem to indicate that employing a higher spatial resolution (36 km) does not significantly improve simulation of precipitation. We speculate that a combination of several physics parameterizations and lack of model tuning gives rise to the observed differences between the models and the observations.

To my grandmother, Narmada Krishnamurthi,

and my kindergarten teacher, Mrs. Janaki Leslie

ACKNOWLEDGMENTS

First of all, I would like to thank my advisor Dr. Kenneth P. Bowman for his invaluable support and guidance, both technically and monetarily, and for being extremely patient with me during my four years as a Ph.D. student. Next, I would extend my heartfelt thanks to Dr. Gerald R. North with whom I enjoyed the various scientific and worldly discussions without which I would not have realized my goals. I would also like to thank my other committee members Dr. R. Saravanan and Dr. Prabir Daripa for their support and encouragement.

I would like to thank my friends and colleagues for their undoubting faith in my abilities and helpful discussions. I am very grateful to our IT support team, particularly Neil Smith and Chris Mouchyn, and also the entire Atmospheric Sciences Department office staff for all their help and support.

I would like to thank the TRMM Scientific Data and Information System (TSDIS) at the NASA Goddard Space Flight Center for providing me with the TRMM data. I would like to express my special thanks to Dr. Ruby Leung at the Pacific Northwest National Laboratory for providing me with the WRF data and also for all her support and encouragement.

Last, but not least, I would like to express my deepest gratitude and thanks to my parents, Ram and Rajyasree, my brother, Govind, and my grandmother, Narmada for all their love and blessings and without whom this would not have been possible.

TABLE OF CONTENTS

Page

LIST OF TABLES

LIST OF FIGURES

FIGURE Page

FIGURE Page

FIGURE Page

FIGURE Page

FIGURE Page

CHAPTER I

INTRODUCTION

One of the major problems that atmospheric scientists face today is the accurate representation and prediction of precipitation. Rainfall spans a wide range of space and time scales; and although the development of faster computers and better analytical models have helped to better simulate this variability, inadequate understanding of some of the fundamental dynamical and microphysical processes of rainfall has slowed progress in the area of quantitative rainfall forecasting. Several research efforts are directed to address this problem, which forms the primary focus of the current study.

From the perspective of the climate system, rainfall is a key component of the hydrological cycle. The presence of water over land determines habitability via its influence on ecological systems through the net of precipitation minus evaporation. Over the oceans rain affects surface salinity and hence mixing processes that influence deep convection (Browning, 1990). The most important impact of rain and its variability is on the biosphere, including human society. Additionally, rain-clouds directly affect the atmosphere through latent heat release by precipitation, two-thirds of which falls in the tropics, and this in turn profoundly influences the general circulation. Therefore, variability in the horizontal distribution and intensity of tropical convection has global effects, as evidenced in the teleconnections of the El Niño-Southern Oscillation (ENSO) phenomenon. (See Ropelewski and Halpert (1987), Montroy (1997), Mo and Higgins (1998), Lau and Wu (2001), and Adler et al. (2000), among others).

Quantitative estimates of tropical precipitation from sources such as rain gauges and ground-based radars suffer from errors as large as 100% due to lack of reliable

---

This dissertation follows the *Journal of Climate*.

direct measurements as well as due to the highly variable nature of rainfall (North, 1987). Thus the only way to collect global-scale rainfall data and accurately account for its variability is by means of space-borne satellite sensors. The Tropical Rainfall Measuring Mission (TRMM) was specifically developed to study rainfall in the tropics by using passive microwave, visible and infrared sensors along with the first space-borne rain radar. With an orbital inclination of 35°, the TRMM satellite is able to view the earth's surface between about 40°S and 40°N and has provided researchers with instantaneous rain-rate measurements throughout the tropics. This will contribute to a better understanding of latent heat release during precipitation, which is a major driver of atmospheric circulation (Kummerow et al. 2000).

Since rainfall fields exhibit large space-time variability, one of the goals of this study is to examine whether a specific space-time covariance structure exists for rainfall. In chapter II, the validity of Taylor's "frozen-field" hypothesis is tested for rainfall fields using four days of high-resolution radar reflectivity data, which is used as a proxy for precipitation. If true, the hypothesis could be used to infer spatial properties of the rainfall field at a particular instant of time from temporal information at a particular location. The Taylor hypothesis is tested using two different statistical approaches, the first being based upon rigorous hypothesis testing, while the second uses a simple correlation analysis. We also construct an analytical diffusion model for rainfall and test the validity of the hypothesis for the same. The results from testing the analytical model serve to reinforce our main conclusions and raise questions about the validity of the hypothesis when applied to precipitation fields as reported by earlier studies (Zawadski 1973; Crane 1990; Poveda and Zuluaga 2005).

In chapter III, the quality of global climate model (GCM) simulations of rainfall variability in the tropics, in terms of long-term time and seasonal means, is tested by comparing model simulations with satellite observations. In most regions of the trop-

ics, the annual cycle accounts for a substantial portion of the variability associated with precipitation and is therefore key to improving our understanding of the physics of the atmosphere. In this regard, simulations of the annual cycle of precipitation by a high-resolution (36-km) numerical model in a tropical channel are compared with a new comprehensive high-resolution precipitation dataset (3B42 V6) from TRMM and other satellites and ground-based instruments. Results from the Community Atmosphere Model (CAM) are also shown for comparative purposes with the primary goal of assessing whether improved spatial resolution leads to greater skill in predicting seasonal rainfall.

CHAPTER II

TAYLOR HYPOTHESIS*

A. Definition

The Taylor hypothesis (TH) as applied to rainfall is a proposition about the space-time covariance structure of the rainfall field. Specifically, it supposes that if a spatio-temporal precipitation field with a stationary covariance $\mathrm{Cov}(\mathbf{r}, \tau)$ in both space $\mathbf{r}$ and time τ, moves with a constant velocity $\mathbf{v}$, then the temporal covariance at time lag τ is equal to the spatial covariance at space lag $\mathbf{v}\tau$, that is, $\mathrm{Cov}(\mathbf{0}, \tau) = \mathrm{Cov}(\mathbf{v}\tau, 0)$. Qualitatively this means that the field evolves slowly in time relative to the advective time scale, which is often referred to as the frozen field hypothesis. Of specific interest is whether there is a cut-off or decorrelation time scale for which the TH holds for a given mean flow velocity $\mathbf{v}$.

Based on studies of turbulent flow, Taylor (1938, p. 478) proposed a simple model of the covariance structure of a turbulent current with a constant mean background velocity. He hypothesized that small-scale turbulence might be carried along by the mean flow in such a way that the temporal covariance of a variable at time lag τ would be equal to the spatial covariance at space lag $\mathbf{r} = \mathbf{v}\tau$, where $\mathbf{v}$ is the mean velocity of the flow. Specifically, consider a stationary spatio-temporal random field $Z(\mathbf{x}, t)$ at spatial location $\mathbf{x} \in \mathbf{R}^d$, $d \geq 1$, and time $t \in \mathbf{R}$. Let $C(\mathbf{r}, \tau) = \mathrm{Cov}\{Z(\mathbf{x}, t), Z^*(\mathbf{x}+\mathbf{r}, t+\tau)\}$ denote its stationary covariance function for spatial lag $\mathbf{r}$ and temporal lag τ. In this case the Taylor hypothesis (abbreviated TH) can be

---

*Reprinted with permission from "Statistical tests of Taylors hypothesis: An application to precipitation fields" by Bo Li, Aditya Murthi, Kenneth P. Bowman, Gerald R. North, Marc Genton and Michael Sherman, 2008. *Journal of Hydrometeorology*, 10, 254–265, ©[2008] American Meteorological Society.

written as

$$C(\mathbf{0}, \tau) = C(\mathbf{v}\tau, 0). \tag{2.1}$$

Note that the mean velocity $\mathbf{v}$ may not be known *a priori*. Although we consider TH in a stationary random field for simplicity, it is worth mentioning that TH can also be defined for a non-stationary random field where the covariance function and velocity $\mathbf{v}$ have to be location specific (e.g., Burghelea et al. 2005). Under all circumstances, TH assumes the existence of a large mean flow compared to the velocity fluctuation, which allows the latter to be frozen into the former. TH is also of interest for many other fields such as the cloud and radiation testbed measurements (Sun and Thorne 1995) other than rainfall.

1. Background

Several studies have attempted to test the TH for atmospheric convection by using radar observations of precipitation. Based on empirical correlations, Zawadzki (1973) argued that Taylor's hypothesis is plausible for precipitation data for temporal lags less than 40 minutes. His results seemed to indicate that spatial correlations exhibited more memory than temporal correlation. That study was based on only 11 radar scans from one radar for a single storm event, so its generality is not known. Gupta and Waymire (1987) and Cox and Isham (1988) studied the validity of the hypothesis for various theoretical space-time covariance models, but did not test the TH with observations. Crane (1990) observed that the TH held in rainfall fields up to a time scale of around 30 min for spatial scales less than 20 km, after which it broke down.

Poveda and Zuluaga (2005) tested the validity of the TH for a set of 12 storms observed in southwestern Amazonia, Brazil, during the January-February 1999 Wet Season Atmospheric Meso-scale Campaign. They concluded that the TH did not hold

in 9 out of the 12 studied storms, but that it did hold for 3 storms up to time scales of around 10-15 minutes. That time scale is related to the life cycles of convective cells in the region. The generality of these results, however, is open to interpretation; and their conclusions are not based on a statistical comparison of the spatial and temporal covariances. This points to the need for a formal statistical testing procedure to assess Taylor's hypothesis and the application of rigorous statistical methods to sizable data sets. Aside from rainfall, the study method may also be useful in investigating the cloud structure and the thermodynamics of moisture transport related to precipitation processes (Sun and Thorne 1995).

In this study we use a rigorous statistical approach to test the TH based on the asymptotic joint normality of covariance estimators derived by Li et al. (2008). The method is applied to high-resolution gridded NEXRAD radar reflectivity data. These results are compared with a simple estimate of statistical significance based on the assumption of independence of the covariance estimates (see Li et al. 2008 for details).

B. Data

As a prototype observational data set to test Taylor's hypothesis, we use high-resolution gridded NEXRAD radar reflectivity data produced by the WSI Corporation. Data from all available operating radars are routinely merged onto a longitude-latitude grid for the conterminous United States with an approximate horizontal resolution of 4 km $\times$ 4 km. The radar reflectivity data are maps depicting the highest reflectivity measured above each grid box computed from scans at multiple elevation angles. Reflectivity values Z are transformed logarithmically using $dBZ = 10 \log_{10}(Z)$ and discretized with 5 dBZ precision from 0 to 75 dBZ. Multiple levels of

quality control to remove ground clutter and false echoes, along with multiple volume scans, which nominally require 5 to 6 minutes, are used to produce gridded analyses with 15-minute temporal resolution (96 time steps per day). For this study we use radar reflectivity in dBZ rather than rain rates. Reflectivity is an observable parameter, so it is physically reasonable to ask whether it obeys Taylor's hypothesis. Calculations using estimated rain rates R yield similar results (further discussion below).

Although atmospheric convection is a three-dimensional phenomenon, we treat the precipitation as two-dimensional by using the radar rainfall composites described in the preceding paragraph. The national radar grids are 3661 $\times$ 1837 grid cells. For our analysis we select a sub-area of the grid and a time period during which there is substantial rainfall. We chose 4 days of gridded radar reflectivities from the southeastern United States (75° to 100°W, 30° to 40°N) for the period 2 to 5 May 2002 (4 days $\times$ 96 time steps/day = 384 times steps). The selected region has 1308 $\times$ 558 grid cells. During this period there are no time steps with complete missing grids, although individual radars may not have been continuously available. A cold front moved into the region from the northwest early in the study period and then became stationary. Multiple mesoscale convective systems propagated eastward along the frontal boundary during the period. A sample radar image is shown in Figure 1(a). Superimposed on the radar image are 500 hPa geopotential height contours from the NCEP reanalysis (Kalnay et al. 1996). An animation of the time evolution of the radar reflectivity and geopotential height is available at http://csrp.tamu.edu/hiaper/archive/Taylor/radar.mov (54 MB). The geopotential height is linearly interpolated in time to the radar analysis times from the 6-hourly NCEP reanalysis.

The time-mean of the radar reflectivity, shown in Figure 1(b), illustrates the spa-

tial heterogeneity of the data during the study period. The highest mean reflectivities occur in the center of the region, while the southern part has few or no echoes. Minor artifacts (circular radar footprints) are visible from the procedure that merges the individual radars into the gridded mosaic. During the period of study the synoptic-scale flow is predominantly westerly, with only weak wave disturbances. The 500 hPa height field in Figure 1(a) is typical. The time-mean zonal and meridional wind components for the study period, averaged over the study area, are plotted in Figure 2 as a function of pressure. Winds are from the NCEP reanalysis, which has $2.5° \times 2.5°$ longitude-latitude resolution. The average directional wind shear is very small during this period, with the flow at levels above the surface generally moving slightly north of east. The mean wind speed increases from the surface up to a maximum of $\sim$42 m s^{-1} near the tropopause at 200 hPa and then decreases at higher levels in the stratosphere. From this we can anticipate that convection, and the observed radar echoes, will propagate approximately eastward with speeds typical of the mid-tropospheric flow speed of $\sim$20 to 30 m s^{-1}.

C. Methods

1. Hypothesis testing

Our method for testing the Taylor hypothesis is developed based on the asymptotic joint normality of sample space-time covariance estimators derived by Li et al. (2008). Assume $Z(\mathbf{x}, t)$ is a strictly stationary space-time random field with covariance function $C(\mathbf{r}, \tau) = \text{Cov}\{Z(\mathbf{x}, t), Z(\mathbf{x} + \mathbf{r}, t + \tau)\}$, where $\mathbf{r}$ and τ denote an arbitrary spatial lag and time lag, respectively. Let $\mathbf{\Lambda}$ be a set of space-time lags such as $\mathbf{\Lambda} = \{(\mathbf{r}_1, \tau_1), ..., (\mathbf{r}_m, \tau_m)\}$ where m denotes the number of its elements. Let $\widehat{C}(\mathbf{r}, \tau)$ denote an estimator of $C(\mathbf{r}, \tau)$. For simplicity, we choose $\widehat{C}(\mathbf{r}, \tau)$ as the moment es-

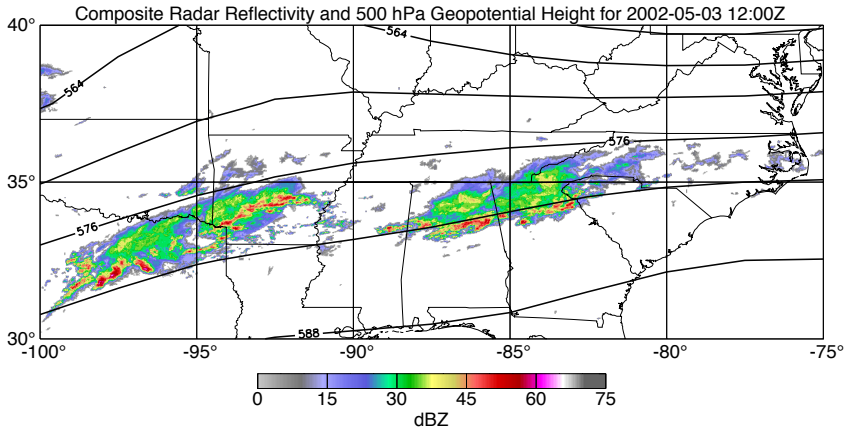

(a)

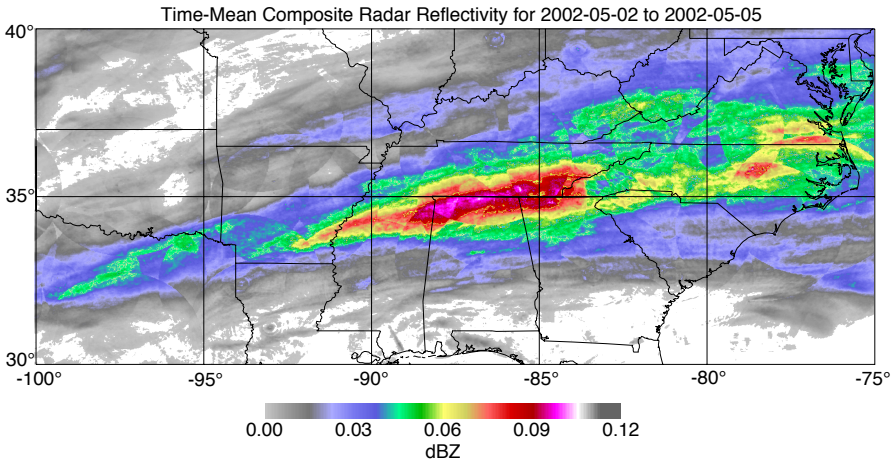

(b)

Fig. 1. (a) Composite radar reflectivity map at 2002-05-03 12:00Z. Contours are 500 hPa geopotential height in dam and (b) Time-mean composite radar reflectivity map for 2002-05-02 to 2005-05-05.

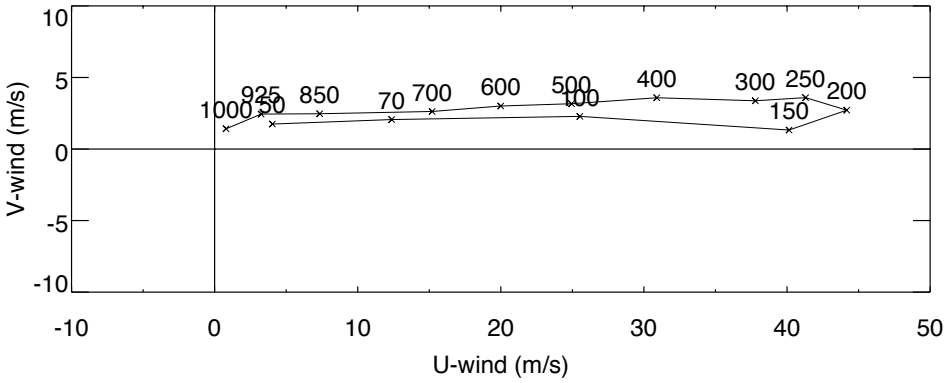

Fig. 2. Time-mean area-mean wind velocity as a function of pressure from the NCEP reanalysis. Labels indicate pressure levels in hPa.

timator defined by $\widehat{C}(\mathbf{r},\tau) = \frac{1}{N}\sum_{\mathbf{x}}\sum_{t}(Z(\mathbf{x},t)-\bar{Z})(Z(\mathbf{x}+\mathbf{r},t+\tau)-\bar{Z})$, where $\bar{Z}$ denotes the mean of $Z(\mathbf{x},t)$ and N is the total number of summands. This choice of estimator works well in testing properties of the covariance function (see Li, Genton and Sherman 2007). Let $\mathbf{G} = \{C(\mathbf{r},\tau), (\mathbf{r},\tau) \in \mathbf{\Lambda}\}$ and let $\widehat{\mathbf{G}} = \{\widehat{C}(\mathbf{r},\tau), (\mathbf{r},\tau) \in \mathbf{\Lambda}\}$ denote the estimator of $\mathbf{G}$. Li et al. (2008) derived that the appropriately standardized and centered $\widehat{\mathbf{G}}$ has an asymptotic multivariate normal distribution in a variety of space-time contexts.

2. Test with a given $\mathbf{v}$

We write Taylor's hypothesis as

$$H_0 : C(\mathbf{0},\tau) - C(\mathbf{v}\tau,0) = 0, \text{ for any } \tau. \tag{2.2}$$

Observe that H_0 is a contrast of covariances and thus can be rewritten in the form of $\mathbf{AG} = \mathbf{0}$, where $\mathbf{A}$ is a contrast matrix of row rank q, say.

For example, if

$$\mathbf{\Lambda} = \{(\mathbf{0}, \tau_1), (\mathbf{0}, \tau_2), (\mathbf{0}, \tau_3), (\mathbf{v}\tau_1, 0), (\mathbf{v}\tau_2, 0), (\mathbf{v}\tau_3, 0)\}, \tag{2.3}$$

then

$$\mathbf{G} = (C(\mathbf{0}, \tau_1), C(\mathbf{0}, \tau_2), C(\mathbf{0}, \tau_3), C(\mathbf{v}\tau_1, 0), C(\mathbf{v}\tau_2, 0), C(\mathbf{v}\tau_3, 0))'. \tag{2.4}$$

Define

$$\mathbf{A} = \begin{bmatrix} 1 & 0 & 0 & -1 & 0 & 0 \\ 0 & 1 & 0 & 0 & -1 & 0 \\ 0 & 0 & 1 & 0 & 0 & -1 \end{bmatrix}, \tag{2.5}$$

then we have $\mathbf{AG} = \mathbf{0}$ under the null hypothesis. Replacing $C(\cdot)$ with the estimator $\widehat{C}(\cdot)$ in (2.2), we obtain a contrast vector for testing H_0 as the estimated left hand side of (2.2), $\mathcal{C} = \widehat{C}(\mathbf{0}, \tau) - \widehat{C}(\mathbf{v}\tau, 0)$. Apparently, $\mathcal{C}$ can be rewritten into the form of $\mathbf{A}\widehat{\mathbf{G}}$. We form the test statistic (TS) based on the contrasts of $\widehat{\mathbf{G}}$ and obtain the distribution of TS under the null hypothesis (Li et al. 2008) as

$$\text{TS} = a_N(\mathbf{A}\widehat{\mathbf{G}})^{\text{T}}(\mathbf{A}\mathbf{\Sigma}\mathbf{A}^{\text{T}})^{-1}(\mathbf{A}\widehat{\mathbf{G}}) \longrightarrow \chi^2_q, \tag{2.6}$$

in distribution as $N \to \infty$, for a matrix $\mathbf{A}$ with row rank q, and an appropriate sequence of normalizing constants a_N. We follow Li et al. (2008) and estimate $\mathbf{\Sigma}$ using subsampling techniques. The choice of subblock size is described in Carlstein (1986). In terms of our precipitation data, the rich temporal replicates allow us to consider the asymptotics in time dimension and form overlapping subblocks using a moving sub-block window along time. Specifically, let N be the total number of time steps, $a_N = \sqrt{N}$ in (2.6), and the optimal block length for sub-blocks is $(2\gamma/1-\gamma^2)^{2/3}(3N/2)^{1/3}$, where γ can be estimated by $\hat{\gamma} = \widehat{C}(\mathbf{0},\, 1)/\widehat{C}(\mathbf{0},\, 0)$. Covariance estimates obtained from each sub-block constitute the sample to estimate $\mathbf{\Sigma}$. The statistical significance of the resulting test statistics can be assessed based on the large sample χ^2 distribution

of the test statistic.

D. Models of the autocovariance function for precipitation

1. Isotropic case

To provide some physical insight into the covariance function for precipitation we develop a simple mathematical model of an evolving precipitation field following Cahalan et al. (1981), North and Nakamoto (1989), Bell et al. (1990), and Bell and Kundu (1996). The model includes propagation (advection), damping, diffusion, and a white-noise stochastic forcing. The evolution of the dependent variable $R(\mathbf{x}, t)$, which represents rain rate, is given by the equation

$$\frac{\partial R}{\partial t} + \mathbf{v} \cdot \nabla R - D\nabla^2 R = -bR + f(\mathbf{x}, t), \tag{2.7}$$

where $\mathbf{v}$ is a constant advective velocity, D is the diffusion coefficient, b is the damping rate, and f is a stochastic forcing term. The analytical solution to this model can be used directly to compute the covariance function.

The equation is solved in the spectral domain $(\mathbf{k}, \omega)$ where $\mathbf{k} = (k_x, k_y)$ is the spatial wavenumber and ω is the temporal frequency. The random forcing $f(\mathbf{x}, t)$ is a stationary Gaussian random variable that is white in both space and time. That is

$$\langle f(\mathbf{x}, t) \rangle = 0 \qquad \text{and} \qquad \langle f(\mathbf{x}, t) f(\mathbf{x} + \mathbf{r}, t + \tau) \rangle = f_0^2 \, \delta(\mathbf{r}, \tau), \tag{2.8}$$

where angle brackets indicate the ensemble mean.

If we define the Fourier transform of $R(\mathbf{x}, t)$ as

$$\tilde{R}(\mathbf{k}, \omega) = \frac{1}{2\pi} \int_{-\infty}^{\infty} \int_{-\infty}^{\infty} \int_{-\infty}^{\infty} R(\mathbf{x}, t) \, e^{-i(\mathbf{k} \cdot \mathbf{x} + \omega t)} \, d^2\mathbf{x} \, dt \tag{2.9}$$

and take the Fourier transform of (2.7) we get

$$\frac{1}{2\pi}(i\omega + i\mathbf{k}\cdot\mathbf{v} + D|\mathbf{k}|^2 + b)\tilde{R} = \tilde{f}, \tag{2.10}$$

where $\tilde{f} = f_0$ is a constant that specifies the magnitude of the white-noise forcing. Solving for $\tilde{R}$ yields

$$\tilde{R}(\mathbf{k},\omega) = \frac{2\pi\tilde{f}}{(i\omega + i\mathbf{k}\cdot\mathbf{v} + D|\mathbf{k}|^2 + b)}\ . \tag{2.11}$$

The variance or power spectrum density S, is the magnitude of the complex solution

$$S(\mathbf{k},\omega) = |\tilde{R}\cdot\tilde{R}^*| = \frac{4\pi^2|\tilde{f}|^2}{(\omega + \mathbf{k}\cdot\mathbf{v})^2 + (D|\mathbf{k}|^2 + b)^2}\ , \tag{2.12}$$

where $\tilde{R}^*$ indicates the complex conjugate. Note that the variance in (2.12) is positive for all $(\mathbf{k},\omega)$ and hence is consistent with the definition of a valid covariance function (Gneiting et al. 2007). Finally, the covariance function in the physical domain is obtained by taking the inverse Fourier transform of S

$$\begin{aligned} C(\mathbf{r},\tau) &= \frac{1}{2\pi}\int_{-\infty}^{\infty}\int_{-\infty}^{\infty}\int_{-\infty}^{\infty} S(\mathbf{k},\omega)e^{i(\mathbf{k}\cdot\mathbf{r}+\omega\tau)}\ d^2\mathbf{k}\ d\omega \\ &= 2\pi\int_{-\infty}^{\infty}\int_{-\infty}^{\infty}\int_{-\infty}^{\infty}\frac{|\tilde{f}|^2}{(\omega + \mathbf{k}\cdot\mathbf{v})^2 + (D|\mathbf{k}|^2 + b)^2}e^{i(\mathbf{k}\cdot\mathbf{r}+\omega\tau)}\ d^2\mathbf{k}\ d\omega, \end{aligned} \tag{2.13}$$

where $\mathbf{r} = (r_x, r_y)$ and τ are appropriate lags in space and time. We solve the ω integral by contour integration by first making a substitution $\omega' = \omega + \mathbf{k}\cdot\mathbf{v}$ and then dropping the prime to simplify the notation. The final integral is obtained as

$$C(r_x, r_y, \tau) = \pi|\tilde{f}|^2 e^{-b\tau}\int_{-\infty}^{\infty}\int_{-\infty}^{\infty}\frac{e^{i[k_x(r_x - u|\tau|) + k_y(r_y - v|\tau|)]}}{(D|\mathbf{k}|^2 + b)}e^{-D|\mathbf{k}|^2|\tau|}dk_x dk_y. \tag{2.14}$$

We first explore the above integral analytically by expanding the complex exponential in (2.14). We then test the validity of TH by examining whether $C(0,0,\tau) =$

$C(u|\tau|, v|\tau|, 0)$ for a specific $\mathbf{v} = (u, v)$ and τ. Evaluating each term separately yields

$$C(0, 0, \tau) = \pi|\tilde{f}|^2 e^{-b|\tau|} \int_{-\infty}^{\infty}\int_{-\infty}^{\infty} \frac{\cos[k_x u|\tau| + k_y v|\tau|]}{(D|\mathbf{k}|^2 + b)} e^{-D|\mathbf{k}|^2|\tau|} dk_x dk_y \tag{2.15}$$

and

$$C(r_x = u|\tau|, r_y = v|\tau|, 0) = \pi|\tilde{f}|^2 \int_{-\infty}^{\infty}\int_{-\infty}^{\infty} \frac{\cos[k_x u|\tau| + k_y v|\tau|]}{(D|\mathbf{k}|^2 + b)} dk_x dk_y. \tag{2.16}$$

The TH holds if (2.15) and (2.16) are equal. i.e.

$$\pi|\tilde{f}|^2 e^{-b|\tau|} \int_{-\infty}^{\infty}\int_{-\infty}^{\infty} \frac{\cos[k_x u|\tau| + k_y v|\tau|]}{(D|\mathbf{k}|^2 + b)} e^{-D|\mathbf{k}|^2|\tau|} dk_x dk_y \stackrel{?}{=} \pi|\tilde{f}|^2 \int_{-\infty}^{\infty}\int_{-\infty}^{\infty} \frac{\cos[k_x u|\tau| + k_y v|\tau|]}{(D|\mathbf{k}|^2 + b)} dk_x dk_y. \tag{2.17}$$

The Taylor's 'frozen-field' hypothesis requires that the turbulent structure of the field being advected (rain in our case) evolves slowly compared to the advective time scale τ. In the model given in (2.7), the evolution of the rain field is controlled by the diffusion operator and the damping. We investigate the covariance function in the limit of negligible diffusion ($D \to 0$). In this limit, the evolution of the rainfall field is controlled entirely by the damping and the stochastic forcing. Taking the limit and canceling like terms we see that

$$e^{-b|\tau|} \int_{-\infty}^{\infty}\int_{-\infty}^{\infty} \cos[k_x u|\tau| + k_y v|\tau|] dk_x dk_y \neq \int_{-\infty}^{\infty}\int_{-\infty}^{\infty} \cos[k_x u|\tau| + k_y v|\tau|] dk_x dk_y. \tag{2.18}$$

These two expressions are identical except for the factor of $e^{-b|\tau|}$ on the left hand-side. That is, the TH is not satisfied for this model because the damping changes the *magnitude* of the correlation field, even if the *shape* does not change as the correlation is advected downwind. Thus, for a model like this it is not possible to satisfy TH, and the space and time covariances will differ in proportion to the exponential of the ratio of the temporal lag τ and the damping time scale $1/b$.

2. Extension to anisotropic case

The degree of anisotropy is controlled by the magnitude of the diffusion term which in the general case has directional dependence and consists of four components, i.e.,

$$\vec{\vec{\mathbf{D}}} = \begin{pmatrix} D_{xx} & D_{xy} \\ D_{yx} & D_{yy} \end{pmatrix}. \tag{2.19}$$

For simplicity, we assume that the diffusion or stretching is only along the two major axes, i.e. $D_{xy} = D_{yx} = 0$. Thus in this case (2.7) can be rewritten as

$$\frac{\partial R}{\partial t} + \mathbf{v} \cdot \nabla R - D_{xx}\frac{\partial^2 R}{\partial x^2} - D_{yy}\frac{\partial^2 R}{\partial y^2} = -bR + f(\mathbf{x}, t). \tag{2.20}$$

We simplify the above equation by dividing throughout by b and scale the resulting equation with the following non-dimensional variables $t^{'} = bt$, $u^{'} = \left(u\sqrt{b/D_{xx}}\right)$, $v^{'} = \left(v\sqrt{b/D_{yy}}\right)$, $x^{'} = \left(x/\sqrt{D_{xx}/b}\right)$ and $y^{'} = \left(y/\sqrt{D_{yy}/b}\right)$ to obtain

$$\frac{\partial R}{\partial t^{'}} + \mathbf{v}^{'} \cdot \nabla^{'} R - \frac{\partial^2 R}{\partial x^{'2}} - \frac{\partial^2 R}{\partial y^{'2}} = -R + f^{'}(\mathbf{x}, t). \tag{2.21}$$

Following an analysis similar to the one outlined in the previous section, we obtain the covariance function for the anisotropic case in terms of non-dimensional parameters as

$$C(r_x^{'}, r_y^{'}, \tau^{'}) = \pi|\tilde{f}^{'}|^2 e^{-\tau^{'}} \int_{-\infty}^{\infty}\int_{-\infty}^{\infty} \frac{e^{i[k_x^{'}(r_x^{'} - u^{'}|\tau^{'}|) + k_y^{'}(r_y^{'} - v^{'}|\tau^{'}|)]} e^{-|\mathbf{k}^{'}|^2|\tau^{'}|}}{(|\mathbf{k}^{'}|^2 + 1)} dk_x^{'} dk_y^{'} \tag{2.22}$$

where $r_x^{'} = \left(r_x/\sqrt{D_{xx}/b}\right)$, $r_y^{'} = \left(r_y/\sqrt{D_{yy}/b}\right)$ and $\tau^{'} = b\tau$. The form of the above covariance function closely resembles that of (2.14); and, not surprisingly, the TH does not hold for this case either.

E. Covariance calculations

The time series of instantaneous area-averaged reflectivity for the study region is plotted in Figure 3. Several periods of heavier rain are apparent, and a period of little rain can be seen on May 5. The analysis methods described above are applied to the entire 4-day period and to the three sub-intervals of heavier rain indicated by vertical lines and labeled Periods 1 through 3 in Figure 3. For each of the periods of analysis, the time mean for that period at each point

$$\overline{dBZ}(\mathbf{x}) = \frac{1}{N}\sum_{t=1}^{N} dBZ(\mathbf{x}, t) \tag{2.23}$$

is removed, and all calculations are done with reflectivity anomalies $dBZ' = dBZ -$

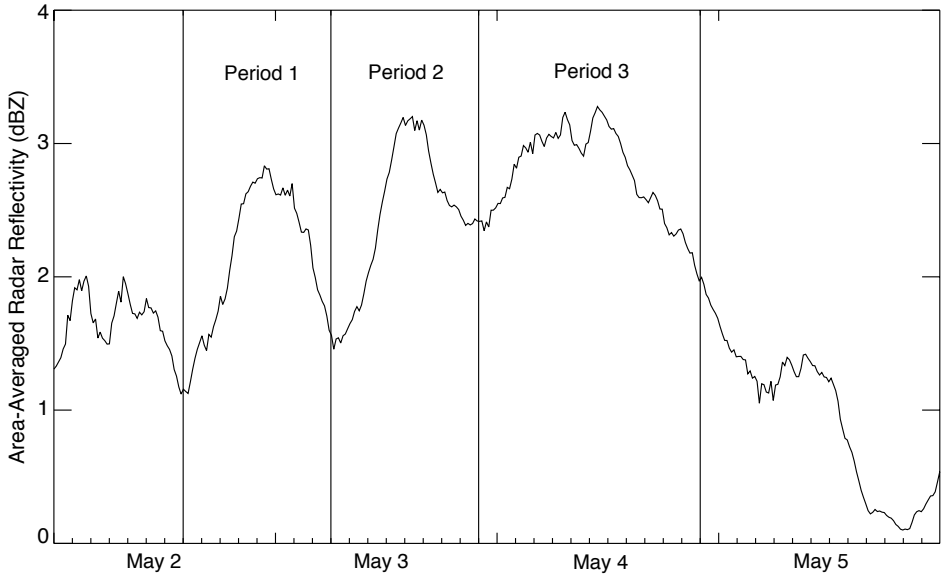

Fig. 3. Time series of area mean radar reflectivity, 2-5 May 2002. The sub-periods selected for the study are: (1) May 2 1400Z - May 3 0600Z, (2) May 3 0600Z - May 3 2200Z and (3) May 3 2200Z - May 4 2200Z. Note here that we do not test TH for May 5 due to little or no rain throughout the domain.

$\overline{dBZ}$. The time-lagged covariance between the reflectivity anomaly $dBZ_i'(t)$ at a reference point (designated by the subscript i) and the anomaly at a test point (designated j) for a given time lag τ is computed using

$$C(\mathbf{r}_{ij}, \tau) = \begin{cases} \frac{1}{N} \sum_{t=1}^{N-\tau} dBZ_i'(t)\, dBZ_j'(t+\tau), & \tau \geq 0 \\ \\ \frac{1}{N} \sum_{t=1-\tau}^{N} dBZ_i'(t)\, dBZ_j'(t+\tau), & \tau < 0 \end{cases} \tag{2.24}$$

where the space lag $\mathbf{r}_{ij} = \mathbf{x}_j - \mathbf{x}_i$ is the vector from point i to point j, and N is the number of observations in the time series. For a given reference point i, $C(\mathbf{r}_{ij}, \tau_n)$ is calculated for all test points j on the data grid within a $2^\circ \times 2^\circ$ rectangular region centered on the reference point (107×113 grid points) and additionally for all time lags (τ_n) from -3 hours to +3 hours. With a time step size of 15 minutes, this amounts to discrete time lag indices (n) between ± 12.

To estimate the average covariance function for the entire domain, $\widehat{C}(\mathbf{r}, \tau)$, we first start off by selecting 2000 random but uniformly distributed reference points throughout the entire domain. The number 2000 is somewhat arbitrary but accurately represents the dataset spatially. Then for each reference point we prescribe the $2^\circ \times 2^\circ$ rectangular region around it and calculate the mean of this region. If this temporally and spatially averaged value is greater than 4 dBZ then we treat the point as a valid reference location otherwise it is rejected. This omits from consideration any reference points where little or no rain fell during the period of analysis. By repeating this process for all 2000 reference points we end up with around 300 *valid* reference locations. Then the calculation in (2.24) is repeated for these 300 locations and then averaged over all locations. Reference points are chosen to be at least 1° away from the boundaries of the domain to avoid edge effects.

Correlations $\hat{c}$ are estimated using

$$\hat{c} = \frac{\widehat{C}}{\hat{\sigma}^2}, \tag{2.25}$$

where $\hat{\sigma}^2$ denotes the estimated variance of the entire precipitation anomaly field. Error bars for $\widehat{C}$ and $\hat{c}$ are roughly estimated by computing the standard deviation of the individual estimates of C or c for the 300 reference points. These correlation estimates based on $\hat{c}$ are then tested for the validity of the TH and are subsequently compared with those from the method described in Section C, which takes into account the correlations between the individual covariance estimates.

1. Structure of the covariance field

The mean space-time covariance function $\widehat{C}(\mathbf{r}, \tau)$ and correlation $\hat{c}(\mathbf{r}, \tau)$ are estimated for the entire 4-day study as described above. The spatial structure of the empirical space-time correlation $\hat{c}$ estimated over all pairs that have the same spatial and temporal lag is shown in Figures 4 and 5. Figure 4 shows contours of $\hat{c}$ as a function of spatial lag at $\tau = 0$, while Figure 5 shows $\hat{c}$ for $\tau = 0$, 15, 30 and 45 minutes. Figure 4 reveals that the $\hat{c}$ has an approximately elliptical shape with the major axis oriented somewhat north of east. The elliptical shape (anisotropy) of $\hat{c}$ indicates the mean orientation of the precipitation areas during this period on the scale shown. As in the theoretical model, the peak observed at $\tau = 0$ (Figure 5a) decays with time as it moves upwind (downwind) with decreasing (increasing) lag (Figures 5b-d).

In order to qualitatively compare the general shape and structure of $\hat{c}$ with that of the anisotropic model (2.20) described in Section D, we also evaluate the model correlation function (2.22) numerically for different values of the parameters $D, b, u, v, \mathbf{r}$ and τ. The goal is not to exactly reproduce the observed values, but to understand the nature of correlation functions with similar shape. Figure 6 illustrates the shape of

(2.22) for $b = 0.25$ minute^{-1}, $u = 1.6 \cdot 10^{-4}$ deg minute^{-1}, $v = 2.5 \cdot 10^{-5}$ deg minute^{-1}, $D_{xx} = 0.20$ deg^2 minute^{-1} and $D_{yy} = 0.075$ deg^2 minute^{-1} for spatial lags (r_x, r_y) that range from -1.0° to +1.0° and temporal lags $\tau = 0$, 15, 30, 45 minutes respectively. While solving (2.14) numerically, the limits of the integration were truncated in order to get a finite correlation function. The shape of the correlation function is similar to the observations. For fields that have this type of covariance structure, with a localized peak in the covariance that decays as it is advected downstream, we generally would not expect the field to satisfy the Taylor hypothesis.

In Figure 4 the maximum correlation at $\tau = 0$ occurs at the origin, as expected. As the magnitude of τ increases from zero in the positive or negative directions, the peak of the correlation function shifts upstream or downstream respectively, depending on the sign of the lag; and the maximum correlation values decrease with increasing lag, as shown in Figure 5. The plus symbols in Figure 4 represent the locations of the peak correlations at time lags of ±15, 30, 45, and 60 minutes. The plus signs are approximately co-linear and equally spaced, indicating that the advective velocity is approximately independent of lag. The average velocity vector $\mathbf{v}$ can be estimated by using the vectors from the origin to the plus signs, divided by the corresponding time lag τ. The mean velocities are found to have magnitudes between 25 and 30 m s^{-1} ($\sim 25.6°$ day^{-1}) oriented ∼83° from north. This is consistent with the mean wind plotted in Figure 3 and with the motion of precipitation features visible in an animation of the radar reflectivity maps. We use this value of $\mathbf{v} = 25.6°$ day^{-1} (83° east of north) to compute $\hat{c}(\mathbf{v}\tau, 0)$ for the entire 4-day period of study. Due to some variability of $\mathbf{v}$ with time, we use individual velocity estimates obtained from the correlation functions for each sub-period when testing the TH for the three sub-periods. Note that the propagation velocity $\mathbf{v}$ and the principal axis of the correlation function c are not oriented in the same direction, nor is there any

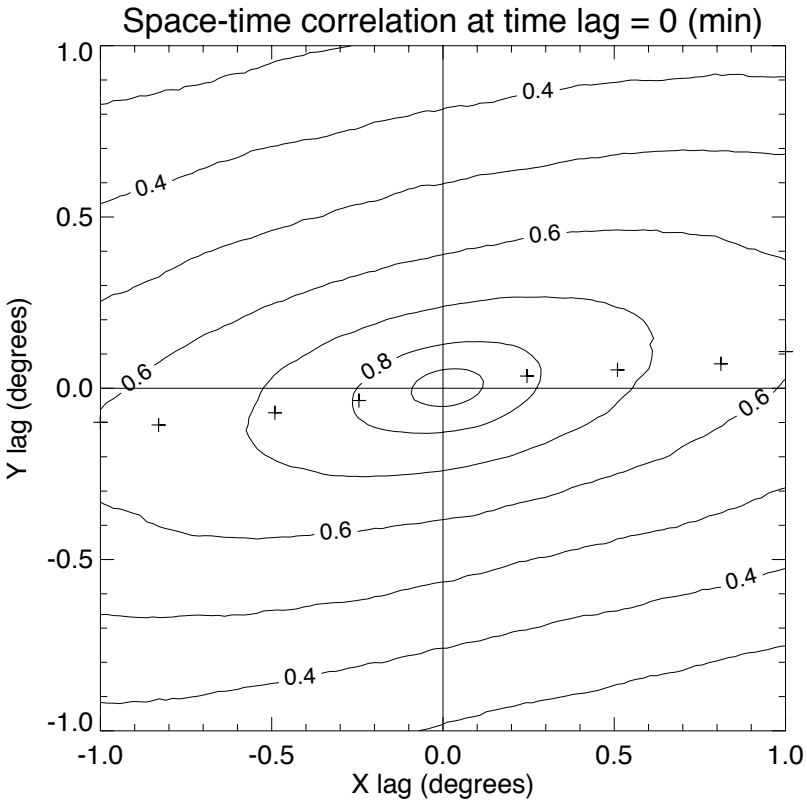

Fig. 4. Averaged space-time correlation ($\hat{c}$) for $\tau = 0$. The plus signs indicate the positions of $\max(\hat{c}(\mathbf{r}, \tau))$ at $\tau = \pm 15$, 30, 45, and 60 minutes, respectively.

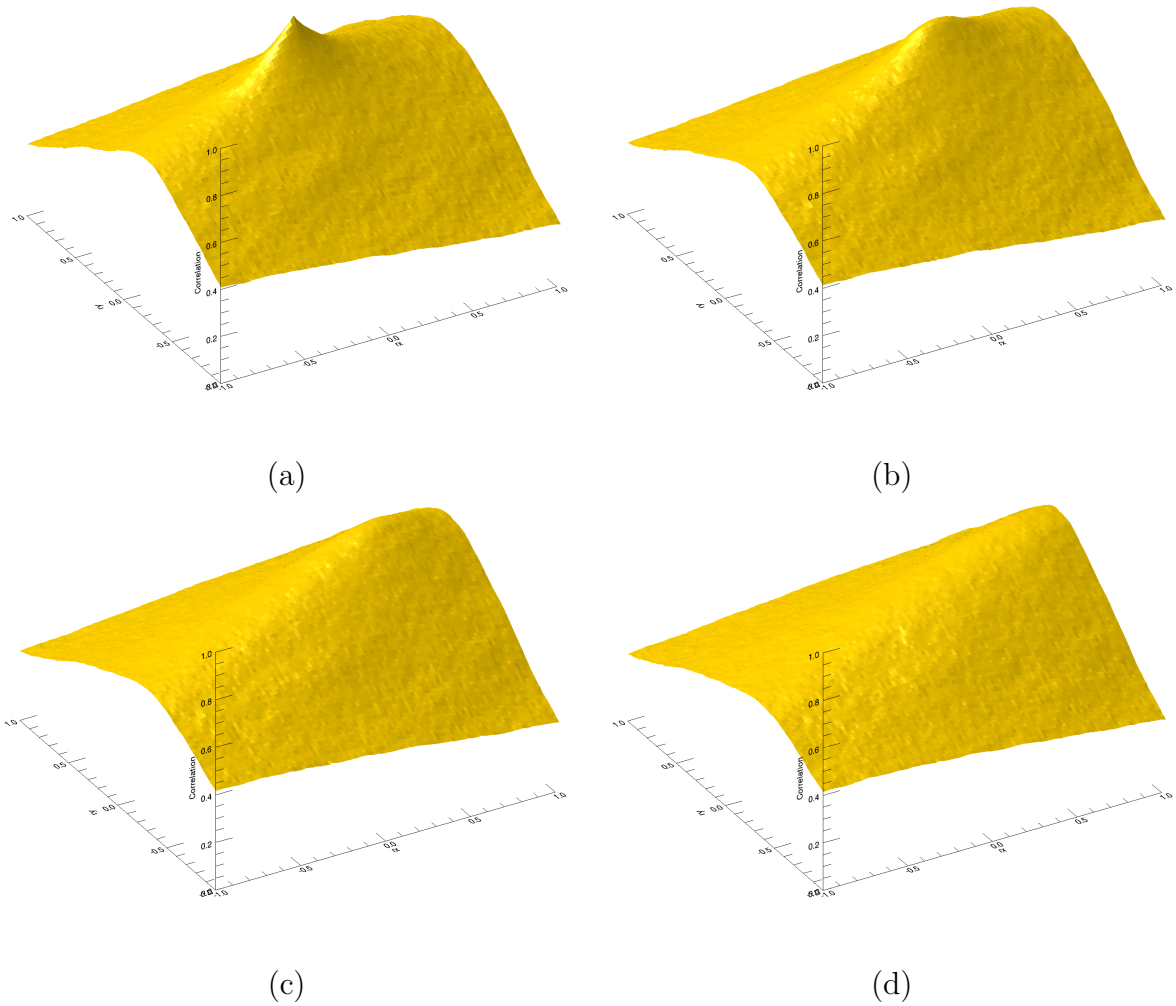

Fig. 5. Averaged space-time correlation fields $\hat{c}$ at (a) $\tau = 0$, (b) $\tau = 15$, (c) $\tau = 30$ and (d) $\tau = 45$ minutes. Isopleths of $\hat{c}$ are approximately elliptical in shape and oriented somewhat north of east (see Figure 1). The field decays in both space and time as it translates with the wind velocity.

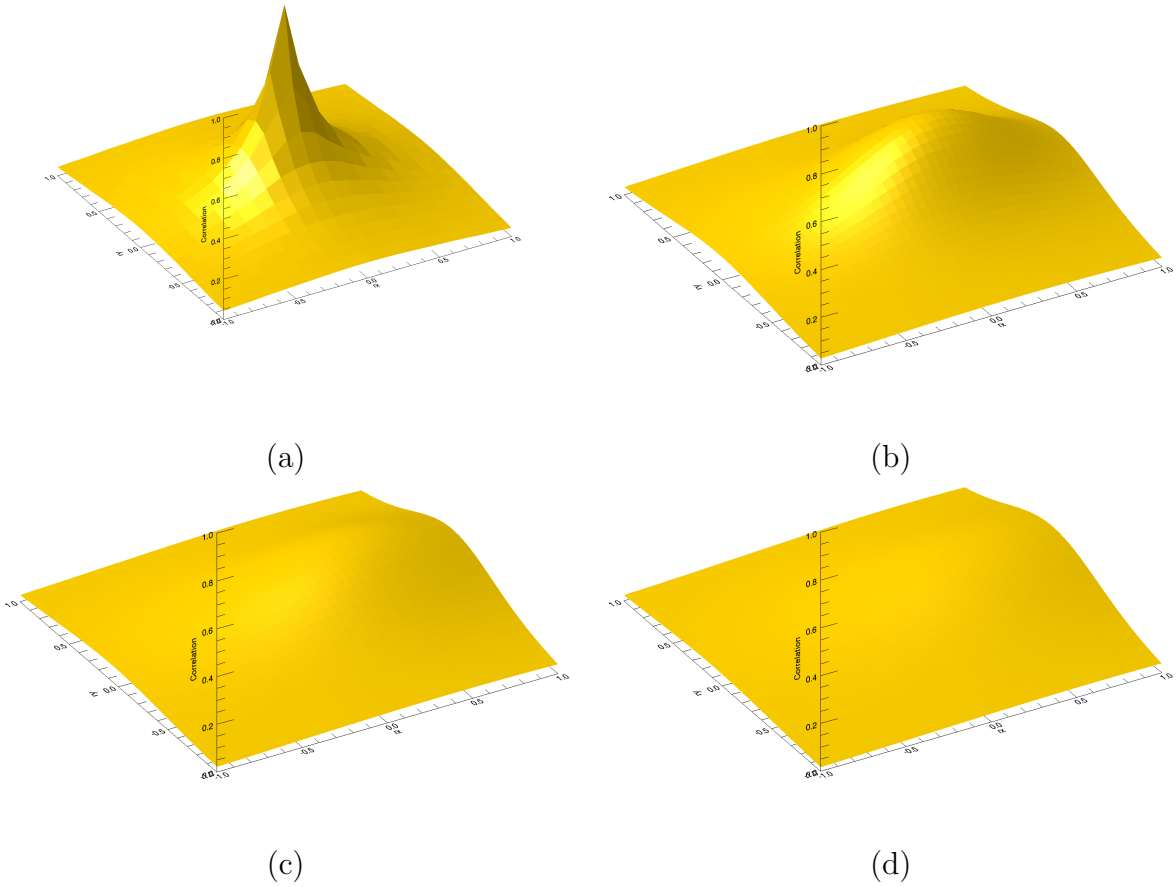

Fig. 6. Correlation fields (cor) for precipitation model (7) at (a) $\tau = 0$, (b) $\tau = 15$, (c) $\tau = 30$ and (d) $\tau = 45$ minutes repectively. It is assumed here that $u = 0.22641°$ day^{-1}, $v = 0.0357°$ day^{-1}, $b = 0.25$ minute^{-1}, $D_{xx} = 0.20$ deg^2 minute^{-1} and $D_{yy} = 0.075$ deg^2 minute^{-1}. The correlation decays as it is advected by the wind in the r_x lag direction.

reason to expect them to be.

F. Testing the Taylor hypothesis

Figure 7 shows the space-lagged correlations ($\hat{c}(\mathbf{v}\tau, 0)$, triangles) and time-lagged correlations ($\hat{c}(\mathbf{0}, \tau)$, diamonds) as a function of time lag for the entire 4-day period plotted on a logarithmic scale. These curves show that the TH in general, does not hold for the 4-day time period and hence for large space and time scales. It is important to mention here that although the curves do appear close (especially at smaller time lags), the error bars (not shown) around the mean correlations corresponding to the shortest time lag of 15 minutes are small and do not overlap thereby indicating that the curves are indeed statistically different. Figure 8 shows curves of correlation plotted as a function of time lag for the precipitation model (2.20). The correlation curves in Figure 8 are similar to those in Figure 7 with the rate of decay being controlled by the magnitude of the damping term b. The conclusions inferred above, is clearly illustrated in Figure 9 which displays correlation plotted against spatial lag at time lags τ =15, 30, 45, and 60 minutes. The correlation at a spatial lag of $\mathbf{0}$ and time lag τ ($\hat{c}(\mathbf{0}, \tau)$), is close to but not equal to the corresponding correlation at $\tau = 0$ and spatial lag scaled by the mean velocity $\mathbf{v}\tau$ (i.e. $\hat{c}(\mathbf{v}\tau, \mathbf{0})$), as indicated by the slight slant in the lines connecting the two estimates.

In addition, we test the TH hypothesis for each of the the smaller time periods illustrated in Figure 10, during which the heaviest rainfall occurs. Figure 10 (a) demonstrates a sub-period for which the TH held up to 15 minutes (35 km) while Figures 10 (b) and (c) show sub-periods for which it did not hold for even short space and time scales.

In order to assess the TH using both methods, a table containing probability

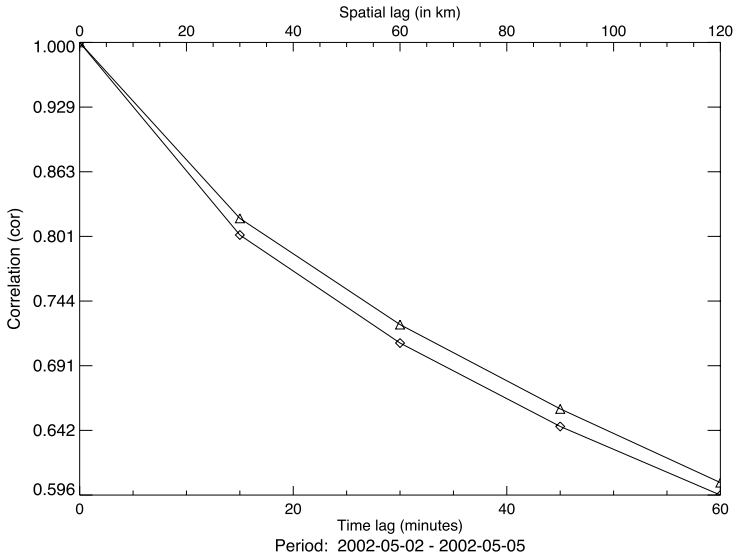

Fig. 7. Averaged space-time correlation ($\hat{c}$) as a function of space and time lags for the entire 4-day period of study. The triangles correspond to $\hat{c}(\mathbf{v}\tau, 0)$ and the diamonds correspond to $\hat{c}(\mathbf{0}, \tau)$ for $\tau = 0, 15, 30, 45, 60$ minutes respectively. The results indicate that the TH does not hold, even for short time intervals.

Table I. Significance p-values at various τ from t-test.

	τ			
Time Period	15 minutes	30 minutes	45 minutes	60 minutes
4-day period	$5.6{\cdot}10^{-4}$	$6.4{\cdot}10^{-5}$	$5.1{\cdot}10^{-6}$	$1.1{\cdot}10^{-3}$
Time Period 1	$\mathbf{4.2{\cdot}10^{-1}}$	$7.7{\cdot}10^{-3}$	$2.5{\cdot}10^{-2}$	-
Time Period 2	$7.8{\cdot}10^{-3}$	$3.4{\cdot}10^{-9}$	0.000	-
Time Period 3	$3.2{\cdot}10^{-9}$	$6.8{\cdot}10^{-7}$	$3.2{\cdot}10^{-5}$	$1.0{\cdot}10^{-2}$

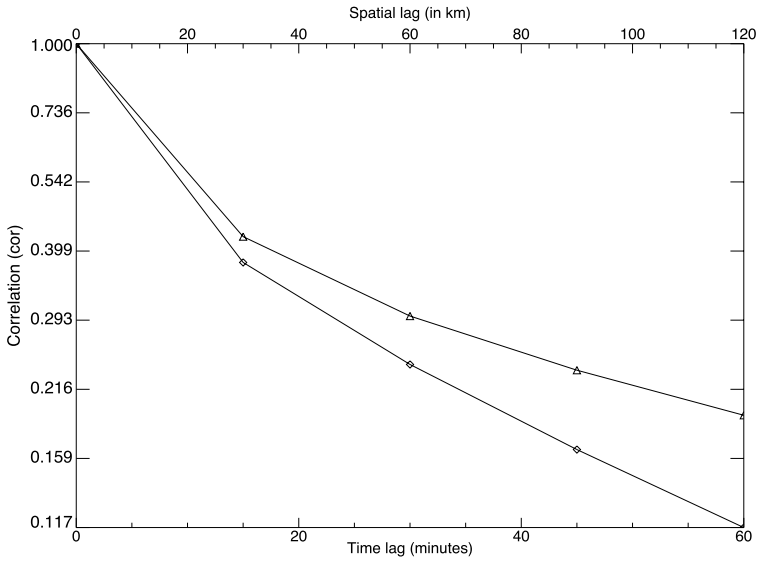

Fig. 8. Space-time correlation (cor) for the precipitation model as a function of time lag. The triangles correspond to $\text{cor}(\mathbf{v}\tau, 0)$ and the diamonds correspond to $\text{cor}(\mathbf{0}, \tau)$ for $\tau = 0, 15, 30, 45, 60$ minutes respectively. These curves serve to reinforce the analytical results described in the paper that the TH does not hold for this model.

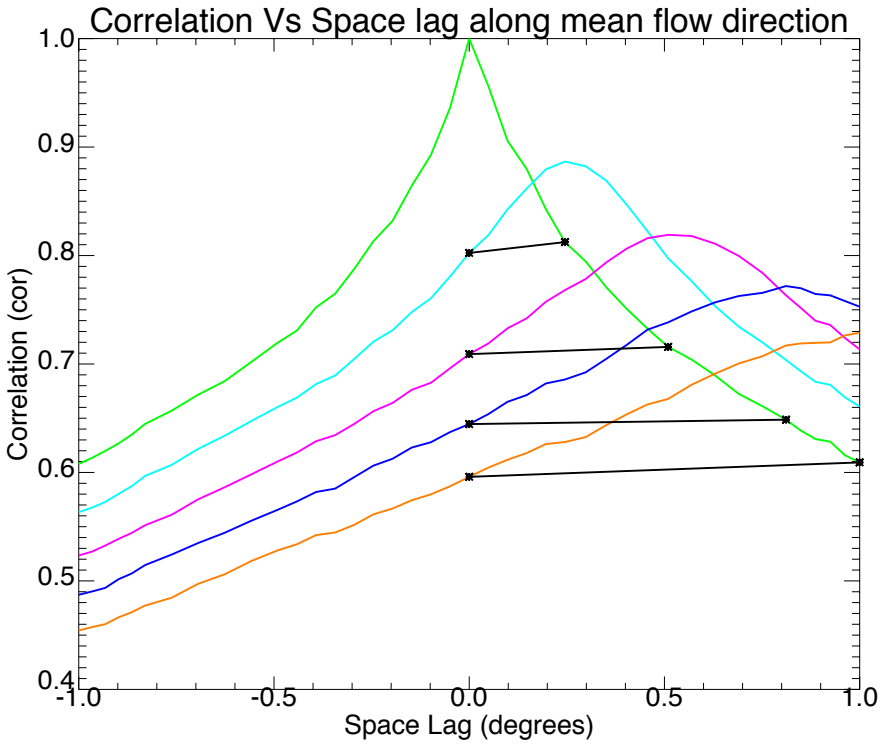

Fig. 9. Averaged space-time correlation ($\hat{c}$) as a function of spatial lag at various time lags $\tau = 0$ and $\pm 15, 30, 45, 60$ minutes as indicated by the colored curves plotted along the mean flow direction for the entire 4-day period of study. The black lines that connect $\hat{c}(\mathbf{0}, \tau)$ and $\hat{c}(\mathbf{v}\tau, \mathbf{0})$ are slightly tilted thus indicating that the TH does not hold for the entire study period.

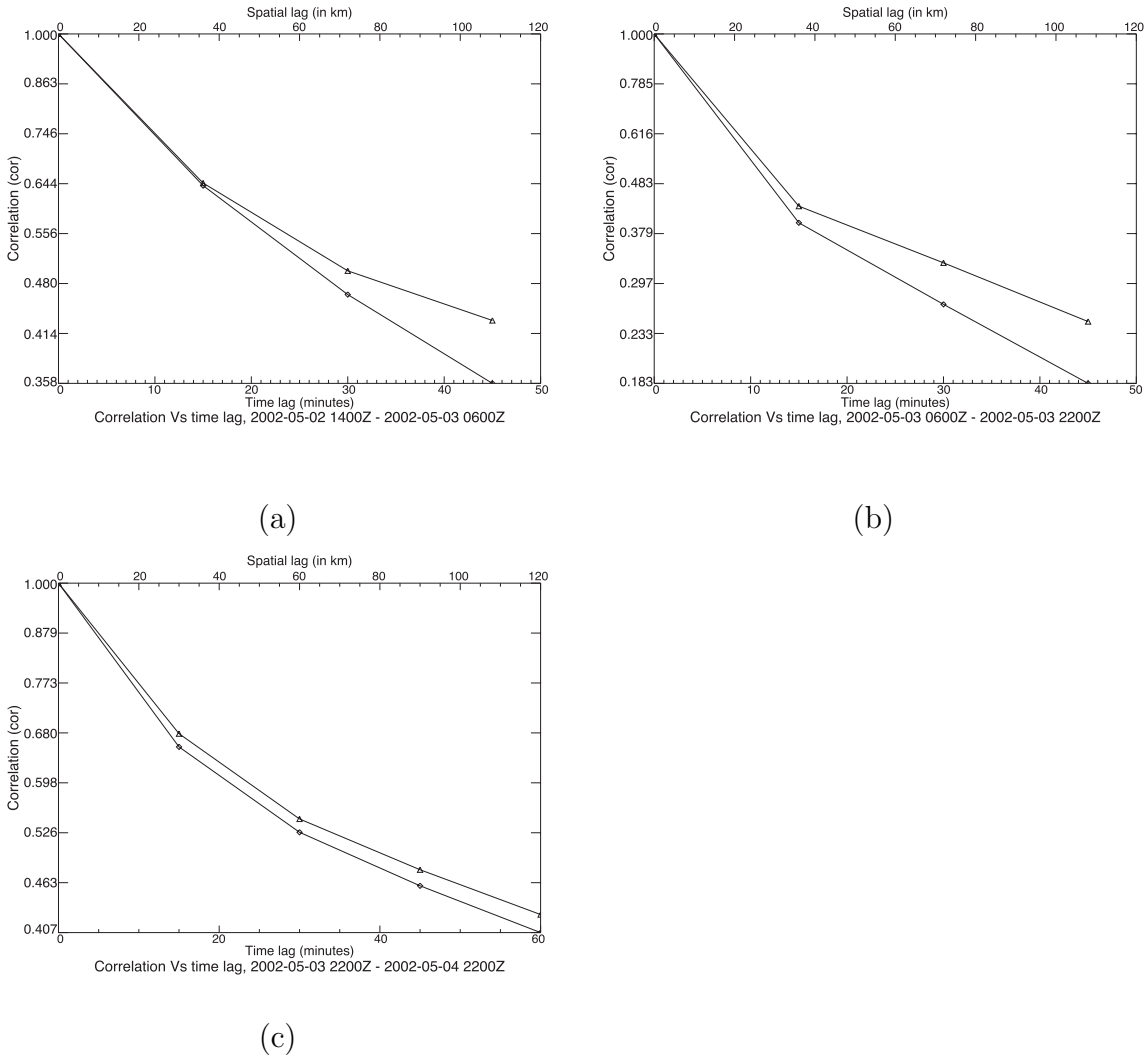

Fig. 10. Averaged space-time correlation ($\hat{c}$) as a function of time and space lags for time period (a) May 2 1400Z - May 3 0600Z, (b) May 3 0600Z - May 3 2200Z and (c) May 3 2200Z - May 4 2200Z. (a) shows that the TH holds for at least 15 minutes (35 km) while (b) and (c) shows that the TH does not hold even for time scales shorter than 15 minutes. Here the Δ's denote $\hat{c}(\mathbf{v}\tau, 0)$ while the $\diamond$'s denote $\hat{c}(\mathbf{0}, \tau)$.

Table II. Significance p-values at various τ from hypothesis testing in Section C.

	τ			
Time Period	15 minutes	30 minutes	45 minutes	60 minutes
4-day period	$5.0{\cdot}10^{-3}$	$1.9{\cdot}10^{-2}$	$4.7{\cdot}10^{-2}$	$2.0{\cdot}10^{-3}$
Time Period 1	$\mathbf{5.8{\cdot}10^{-1}}$	$1.0{\cdot}10^{-3}$	0.000	0.000
Time Period 2	$2.3{\cdot}10^{-2}$	0.000	0.000	0.000
Time Period 3	$1.1{\cdot}10^{-4}$	$7.2{\cdot}10^{-5}$	$2.0{\cdot}10^{-4}$	$3.7{\cdot}10^{-4}$

values (p-values) pertaining to the statistical significance of the difference between the averaged correlations, i.e. $\hat{c}(\mathbf{0}, \tau) - \hat{c}(\mathbf{v}\tau, 0)$, is constructed for each testing period at various time lags using both a standard t-test and the method from Section Ca. These tables serve to reinforce the results illustrated in the Figures 8, 10 (a), (b), and (c) in that the TH does not hold for such systems. Table I lists p-values generated using the t-test, while Table II lists those generated using the method of Li et al (2007). The convention used here is that a p-value $p^* \geq 0.05$ implies that the difference is not significant at the 5% level, and the TH cannot be rejected, while $p^* < 0.05$ indicates that the difference is significant at the 5% level and the TH is rejected. The results from both statistical methods show that the TH does not hold for the full 4-day period, but is admitted for up to 15 minutes (35 km) for one sub-period (Period 1) as indicated by large p^*-values (in 'bold'). The TH is not rejected in only one of the 16 period and lag combinations tested. Although the results from the two methods agree in all cases, it is important to note that the results from the t-test (Table I) tend to overestimate the significance at a particular τ compared to the method of Li et al. (2007) (Table II). This can be attributed to the inability of the correlation method to account for the correlation between the correlation estimates or, equivalently, to

overestimating the number of degrees of freedom. Using the standard NEXRAD Z-R relationship ($Z = 300R^{1.4}$), space-time correlations were also computed using rain rates in order to gauge whether the choice of variable affects the conclusions. The statistical significance of the results has the same pattern as in Table I. In only one case is the TH not rejected (Period 1 at 15 minutes), from which we conclude that the TH does hold for this period up to 15 minutes (35 km). In Table I, p^*-values for time periods 1 and 2 have not been shown for $\tau = 60$ minutes since the velocity estimates for either case resulted in computing locations (and corresponding correlation estimates) that were beyond the $2^\circ \times 2^\circ$ moving window in the spatial domain. The hypothesis testing approach (Table II) however, used a slightly larger moving window and thus reported correlations (and hence p^*-values) at $\tau = 60$ minutes as well.

G. Summary and discussion

Taylor's hypothesis provides a simple model of the covariance function for fluid variables in a uniform flow. It also implies a relationship between the time scale of small scale variations in the fluid compared to the advective time scale of the mean flow. This study compares two approaches to testing the validity of the TH for a geophysical fluid flow by using radar observations of rainfall. The first is based upon a statistically rigorous procedure (Li et al. 2007) while the second is based upon the assumption of independence of the covariance estimates, which demonstrably does not hold in this case. The first method does not require any assumptions about the data distribution and tests the null hypothesis, given by $H_0 : \hat{C}(\mathbf{0}, \tau) - \hat{C}(\mathbf{v}\tau, 0) = 0$ for the mean advection velocity $\mathbf{v}$ and time lag τ. The results indicate that both methods agree well with the analytical model described in Section D in that the TH does not hold for fields characterized by advection, diffusion and decay. The TH does

appear to hold in one case out of sixteen (Period 1 for a lag of 15 minutes), but testing at the 5% level, we would expect this in one case out of twenty. Nevertheless, there is the possibility that the TH might hold for shorter spatial and temporal scales than what is resolved by the data (4 km and 15 minutes). The simple t-test tends to overestimate the significance of the difference between correlation estimates by not accounting for the correlation between those estimates. This is reflected by the fact that the p-values from the t-test are considerably smaller than those obtained by the hypothesis testing procedure in Section C.

The failure of the Taylor hypothesis for the data analyzed here could be due to several factors. First, the background flow velocity $\mathbf{v}$ may not be constant in space or time (Poveda and Zuluaga 2005), although in this case the flow is relatively steady during the study period. Second, the observed variable may evolve with a time-scale shorter than the advection time scale (Waymire et al. 1984). In either case, the results in this paper raise questions about the validity of the TH for radar rainfall data as reported previously by Zawadski (1973) and Poveda and Zuluaga (2005), at least for the space and time scales resolved by the data used here.

CHAPTER III

ANNUAL CYCLE OF PRECIPITATION

A. Introduction and background

The annual cycle of precipitation is a good yard stick for evaluating climate model performance because the seasonal radiative forcing is deterministic and periodic, and the seasonal cycle is a large and easily observed component of precipitation variability. It is forced primarily by the seasonal cycle of solar radiation and corresponding surface fluxes (over land) along with influences from nearby oceans. The annual cycle is known to be large around the tropical Atlantic compared to inter-annual fluctuations of sea-surface temperature (SST) as reported by Biasutti et al. (2003). They found the role of the annual cycle of SST in regulating precipitation to be quite significant over the tropical Atlantic Ocean, along the Guinea coast of Africa and north-eastern Brazil. Gadgil and Sajani (1998) analyzed the seasonal cycle of precipitation in the Atmospheric Model Inter-comparison Project (AMIP) runs and showed that the models that were able to realistically simulate the seasonal transition of rain bands over the Asia-Pacific region were more adept at simulating the seasonal mean pattern of rainfall. Nanjundiah et al. (2005) examined the differences between the seasonal cycle of rainfall over India in the Community Climate System Model (CCSM2) and CAM by using a diagnostic model and found that CCSM2 was able to simulate seasonal rainfall variability better than CAM. This was attributed to a large accumulation of vertically integrated water-vapor in CAM in the pre-monsoon months that gave rise to large rainfall magnitudes throughout peninsular India during the monsoon. Fu et al. (2001) studied the influence of tropical SSTs in modulating the seasonal distribution of monsoon precipitation over South America in CCSM2 and found that the

SSTs affected the Amazon precipitation significantly during the two equinoxes and less during the solstice seasons.

The aim of the current study is to assess the ability of two climate models to simulate this dynamically "forced" component of climate variability (i.e. the annual cycle) via comparisons with satellite observations of rainfall. The ability of climate models to produce precipitation patterns that closely match the observations can serve as powerful tools for diagnosing the reasons behind the shortcomings of current models, and guidance in the investigation of inter-annual variability (Biasutti et al. 2004). Moreover, the success of the models in accurately predicting such long-time behavior would depend upon whether they are capable of simulating the proper interaction between a number of precipitation producing phenomena such as synoptic storms, convective complexes, upslope enhancement, and tropical weather systems (Boyle 1998). For our comparisons with model simulations, we use rainfall data from the TRMM Multisatellite Precipitation Analysis (TMPA 3B42) (see Huffman and Bolovin 2008 for details), that has been produced by combining rainfall information from TRMM and other satellites and ground-based instruments. It is our belief that the TMPA dataset is of high quality and compares well with other contemporary gridded satellite products such as Global Precipitation Climatology Project (GPCP), Climate Prediction Center (CPC) Merged Analysis of Precipitation (CMAP) etc. Thus, it serves as a measure of model performance in simulating precipitation in the present study.

The chapter is organized as follows. In section B, we present a summary of the data corresponding to both satellite observations (TMPA 3B42) and model simulations (Weather Research and Forecast and Community Atmosphere Model). We outline the methodology used to obtain the space-time averaged time means and also the amplitude and phase of the annual harmonic in section C. Section D describes

some of the important results from the comparative study of the annual cycle over four land regions and section E summarizes our results and outlines directions for future research.

B. Data

1. Satellite data

This study uses the TMPA 3B42 data-set to validate model simulations. The data-set comprises of precipitation rates derived from the TRMM Microwave Imager and Precipitation radar aboard the TRMM satellite (see Kummerow et al. 1998) that have been combined with rainfall data from the Special Sensor Microwave/Imager on board the Defense Meteorological Satellites, the Advanced Microwave Scanning Radiometer for Earth Observing System provided by the Japan Aerospace Exploration Agency, the Advanced Microwave Sounding Unit on board NOAA satellites and rain-gauge adjusted microwave-IR rainfall estimates from Geostationary Earth Observing satellites. The physically based microwave estimates are taken "as is" where available, and the remaining grid boxes are filled with IR estimates. Grid boxes where neither μ-wave or IR estimates are available are termed as "missing". These rainfall rate estimates are averaged onto $0.25^\circ \times 0.25^\circ$ latitude-longitude boxes between 50°N and 50°S and calibrated against monthly rainfall estimates from rain-gauges and scaled to 3-hourly temporal resolution. The 3-hourly temporal resolution here does not mean that the satellite sampled rainfall every three hours, but rather pertains to a 3-hour interval or period within which at least a single measurement was made over a given grid box.

Since most rainfall events have short correlation times, typically on the order of a few hours, adequate sampling of rainfall over a given location is required to completely

describe the temporal variability of rainfall. The inadequate nature of the TRMM satellite's sampling pattern introduces an error in the retrieval, relative to ground truth, known as "sampling error". Sampling error has been studied by various researchers who primarily focussed on reducing the uncertainty associated with rainfall retrieval (see Shin and North (1988), Bell and Kundu (1996), Bell and Kundu (2000), Bell et al. (2001) and Bowman (2004), for example). Shin and North (1988) found the TRMM sampling errors in monthly-mean rain rates in wet areas of the Tropics to be less than 10% when averaging observations over areas of $5^\circ \times 5^\circ$. The results of Bowman et al. (2003) showed that very-long-term averages of satellite-derived rain rates compare remarkably well with those measured by rain gauges on areas as small as $1^\circ \times 1^\circ$. Since the dataset used in this study is a merged high-resolution multi-satellite gridded product, we expect the sampling error to be negligibly small, especially when averaged over larger ($\sim 1.4^\circ \times 1.4^\circ$) grid boxes.

2. Weather research and forecast model simulations

Climate simulations have been performed for a period of six years (January 2000 - December 2005) using a tropical channel model that was developed at the National Center for Atmospheric Research (NCAR) based on the WRF model, known as the Nested Regional Climate Model (NRCM). The model is initialized using NCEP/NCAR global reanalysis data, which are also used to force the model at its lateral boundary. Monthly-mean sea surface temperatures (SST) from the Atmospheric model intercomparison experiment (AMIP II) are used as the lower boundary conditions. The model uses the Kain-Fritsch scheme to parameterize cumulus convection (Kain 2004), the radiation scheme from CAM (see Collins et al. 2006) to represent radiative processes in the atmosphere, the WRF Single moment 6-class (WSM6) scheme to explicitly resolve water vapor, cloud and precipitation processes (Hong et al. 2004),

and the Yongsei University (YSU) scheme to calculate transport of fluxes from the planetary boundary layer (Hong et al. 2006). The spatial domain is restricted to the tropical latitudes between 45° S to 45° N, and the model has a resolution of 36 km that translates to $\sim 0.32^\circ \times 0.32^\circ$ on a regular latitude-longitude grid. The model top is at 50 hPa with 56 vertical levels. Both convective and large-scale precipitation are saved as hourly accumulations. Since the model time step is about 4 minutes, each hourly accumulation is the sum of 15 time steps. For this study, we present results from a single NRCM run. From here on we use WRF to mean NRCM for convenience.

3. Community atmosphere model simulations

We also analyze a typical simulation with the Community Atmosphere Model (CAM) for the same six year period at a spatial resolution of T85 ($\sim 1.4^\circ \times 1.4^\circ$) wherein rainfall rates are saved at hourly intervals. The model is forced at the lower-boundary by a weekly-mean SST boundary conditions dataset that spans the six year study period. These were generated by combining SST data from NOAA SST analysis (see Reynolds and Smith, 1994) and from the TMI instrument on board the TRMM satellite. Additionally, the model also requires a time-variant ozone mixing ratio dataset and an initial conditions dataset that includes initial values of prognostic variables. The Zhang-McFarlane (1995) scheme is used to represent cumulus convection. Details about the CAM model can be obtained from Kiehl et al (1996).

Climate models are known to exhibit considerable internal variability or noise, in part due to fluctuations on synoptic time scales. Barnett (1995) showed in his GCM simulations that a single model simulation of a climate forecast is not sufficient for accurate evaluation of model performance. In order to distinguish between the model's response to natural variations in the SST boundary conditions (external variability)

and its response to its own internal variability, it is helpful to look at statistics from an ensemble of simulations. Although extended-range forecast models are considerably sensitive to initial conditions (Lorenz, 1963; Tracton and Kalnay, 1993), the actual initial conditions are largely irrelevant to climate forecasts (Barnett, 1995), since a climate simulation "forgets" its initial conditions after a relatively short interval of deterministic predictability. In this regard, a three member ensemble with different initial conditions but forced with exactly the same sea surface temperature boundary conditions has been used to make the comparisons with WRF and TRMM. The initial conditions for the individual ensemble members were generated from a 10-year control run that used climatological monthly-mean Hadley SSTs as their boundary conditions and were saved at monthly temporal resolution. The initial conditions between the ensemble members differ only in their start dates. For example, the first member was initialized using initial conditions pertaining to October 1, 1999 with a two month spin-up time and data was saved at hourly frequency thereafter. It is important to mention that inter-member correlations are never exactly zero since the same sea surface temperature field is used to force all three members. Results pertaining to a single ensemble member are shown here in order to make reasonable comparisons with WRF.

C. Method of analysis

The long-term time means are calculated by first averaging all 3-hourly (TMPA) and hourly (WRF and CAM) time-steps for the entire six-year period, on the native grid. The TMPA and WRF time means are then interpolated onto the coarsest grid resolution (T85), in order to make reasonable comparisons with CAM. We use harmonic analysis to study annual precipitation patterns since it provides information about

the spatio-temporal variation of precipitation and helps delineate the geographical extent of the various precipitation regimes (Kirkyla and Hameed, 1989). The basic idea involves fitting a statistical model of the annual cycle to the monthly mean rainfall time series at each grid point. Thus, the satellite observations and model data are first binned by month for the six year study period, and then averaged to produce a 12 point representation of the annual cycle. The data (TMPA and WRF) is then interpolated onto a T85 grid.

The procedure outlined above is described below. Specifically, the monthly mean time series at a given location is fit to the following model:

$$r(t_i) = A_0 + \sum_{k=1}^{2} a_k \ \cos\left(\frac{2\pi k t_i}{12}\right) + b_k \ \sin\left(\frac{2\pi k t_i}{12}\right) + \epsilon(t_i) \tag{3.1}$$

where $t_i = (0.5, 1.5, 2.5, \ldots, 11.5)$ is the time in months. A_0 is the mean of the time series, $k = (1, 2)$ is the harmonic index that corresponds to the annual/semi-annual harmonic respectively, and $\epsilon(t_i)$ is the residual of the fit that is assumed to be a normally distributed random variable with zero mean and constant variance. The harmonic coefficients A_0, a_k and b_k are estimated via linear-least squares regression by minimizing $\sum \hat{\epsilon_i}^2$, where $\hat{\epsilon_i}$ are the estimated residuals from the fit of the model. Previous studies have shown that the annual harmonic accounts for a large portion of the precipitation variability over most regions of the globe. However, the semi-annual harmonic is also significant in certain regions and therefore cannot be neglected, but higher harmonics can generally be ignored.

The amplitude (A_k) and phase (ϕ_k) of the annual/semi-annual cycles can be calculated from the estimated coefficients as

$$A_k = \sqrt{a_k^2 + b_k^2} \qquad \phi_k = \tan^{-1}\left(\frac{b_k}{a_k}\right) \tag{3.2}$$

The statistical significance of the estimated coefficients is evaluated using the F-statistic with numerator and denominator degrees of freedom 2 and 12 - 5 = 7 for the annual harmonic and 2 and 12 - 9 = 3 for the semi-annual harmonic (Anderson, 1971). The harmonic vector maps described in following section, are all plotted at the 95% confidence level. It is worth noting that the residuals (ϵ_i) of the fit to the analytical model in (3.1), are normally distributed as inferred by Bowman (2004).

D. Results and discussion

In this section, the fidelity of the climate model's simulation of both long-term time means and the annual cycle of rainfall over land regions is compared against the observations. The objective here is to identify biases (with repect to the observations) in the simulated seasonal mean precipitation and to provide explanations for the same by closely examining errors in the large-scale circulation. The differences between the models and the observations will be referred to as "anomalies" from here on.

1. Climatological long-term means

Fig. 11(a) shows the TMPA six-year mean rain rates plotted on the native grid ($0.25^\circ \times 0.25^\circ$). Figs 11(b) and (c) display the long-term mean anomalies between WRF/CAM and TMPA, respectively, plotted at T85 resolution. In terms of the geographical distribution of precipitation, both models produce considerable biases in regions with significant rainfall. For example, both models overestimate precipitation amount by about 6 mm/day in the western Pacific warm pool region south of the equator.

In the north western Pacific, WRF produces a pronounced rainfall maximum while CAM produces means that are closer to the observations. WRF underestimates

rainfall over most land regions but performs better than CAM over the Arabian peninsula, equatorial and east Africa, and the Arabian sea. WRF also simulates rainfall associated with the Inter-tropical Convergence Zone (ITCZ), fairly accurately over much of the western and central Pacific but produces a large wet bias in the eastern Pacific. On the other hand, CAM produces a large ($\sim$ 6 mm/day) dry bias along the mean latitude of the ITCZ ($\sim 7^\circ$ N) over the central and eastern Pacific. In particular, the ITCZ appears to have shifted north in both models thereby underestimating rainfall over the Panama Bight region. Other notable biases include the substantial dry bias ($\sim$ 3 - 6 mm/day) produced by WRF over major monsoon regions of peninsular India, the Amazon, western equatorial Africa and the maritime continent.

By contrast, CAM produces too much rainfall over the Indian sub-continent and equatorial east Africa, while producing differences similar to WRF in the other regions. For example, there appears to be a substantial net positive mean rainfall anomaly over most of the Arabian sea (see Fig. 11(c)) that leads to an overestimation of monsoon rainfall over much of the sub-continent. Similarly a weak positive rainfall bias exists over southern Africa, that contributes toward a wetter than normal rainy season as described in Section D2b. In general, the magnitude of the differences between mean rainfall produced by WRF and TMPA are around $2 - 4$ mm/day, and are smaller than those between CAM and TMPA, with CAM overestimating rainfall by as much as 6 mm/day over dry regions of the Arabian peninsula and north western India. Both models do a poor job of simulating rainfall associated with the mid-latitude storm tracks along the western edges of the Pacific and Atlantic oceans.

The biases described above are clearly seen in the zonally averaged sections (Fig. 12), calculated for various regions of the global Tropics. The northward shift of the ITCZ is clearly visible in both models over the eastern Pacific (Fig. 12(d)), and over the tropical Atlantic in CAM (Fig. 12(e)). It is worth noting that while WRF

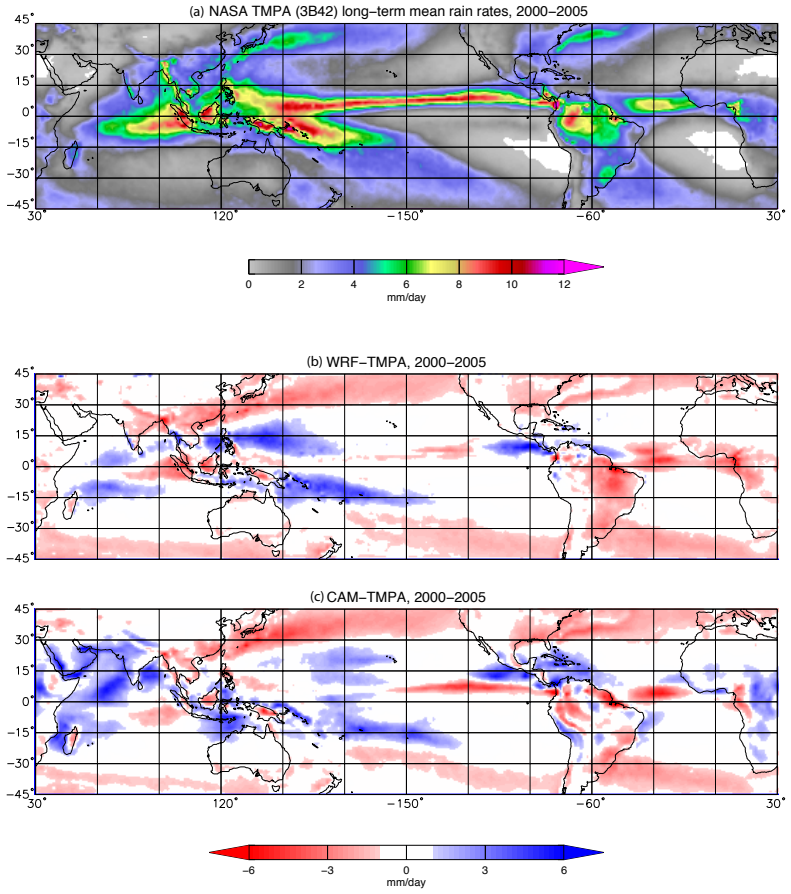

Fig. 11. Six-year long-term mean rain rates for (a) TMPA, (b) WRF and (c) CAM. Blue indicates 'wet' biases, while red indicates 'dry' biases.

significantly underestimates mean rainfall over most tropical land regions, it performs much better over tropical oceans (Fig. 12(b) - (e)) by producing means that are closer to the observations. In the following section, an attempt is made to quantify some of these biases by looking at the seasonal cycle of rainfall on a regional basis.

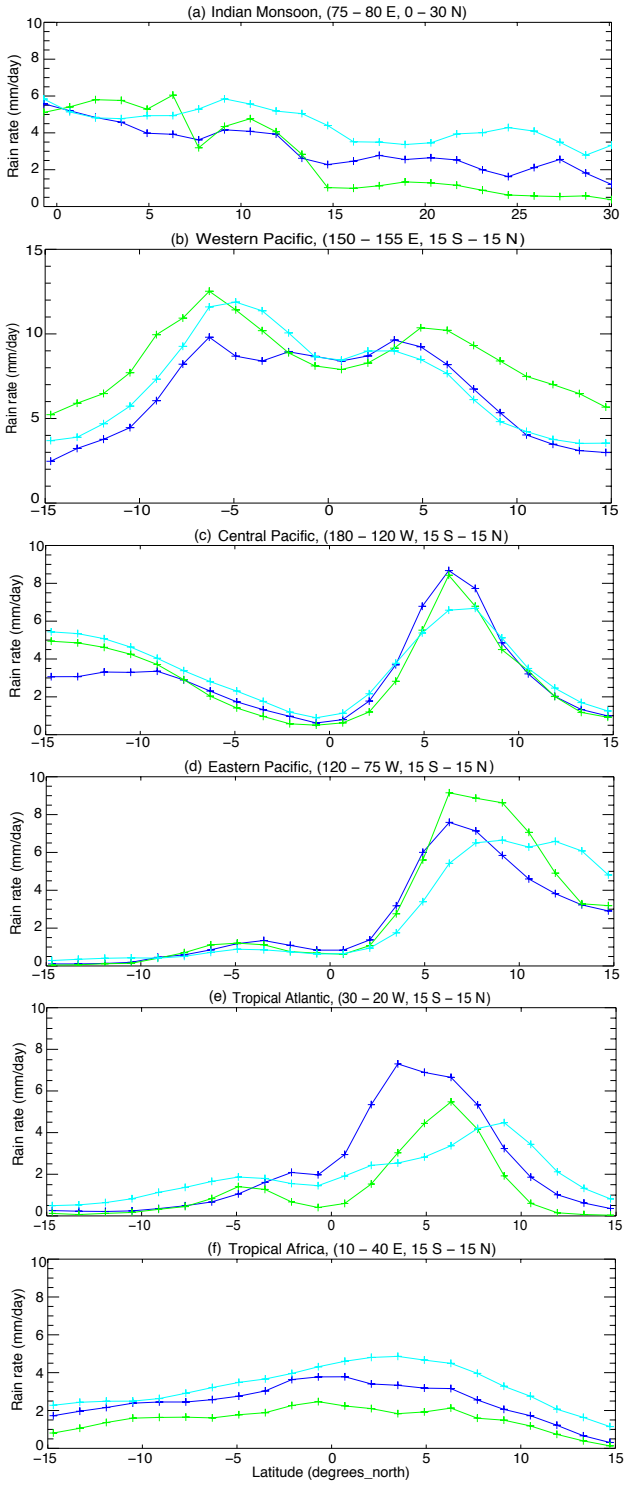

Fig. 12. Zonally averaged long-term time mean rain rates over (a) Indian subcontinent, (b) western Pacific, (c) central Pacific, (d) eastern Pacific (e) tropical Atlantic and (f) tropical Africa. TMPA is plotted in blue, WRF in green and CAM in cyan.

2. Annual cycle

The annual cycle over land is forced locally by the direct effect of solar insolation, and remotely by large-scale circulations that derive their energy from regions of persistent precipitation organized primarily by SST, and secondarily by land (Biasutti et al. 2003). This distinction can be applied to major monsoon regions as well, since the monsoons are driven by land-sea temperature contrasts. The following sections compare the annual cycle of precipitation simulated by the models with the observations. The results have all been spatially averaged onto a T85 grid for comparative purposes.

a. Indian monsoon region

The south-east Asian or Indian monsoon is characterized by an annually reversing wind system that comprises of strong westerlies at the 850 hPa level over the Arabian sea, known as the low-level westerly jet (Goswami et al. 2005). In general, monsoon rainfall over India and its accompanying winds can be attributed to the northward seasonal migration of the east-west oriented rainfall belt (ITCZ) from the southern hemisphere in winter to the northern hemisphere in summer (Gadgil 2003). Some of these features are readily visible in the results described below.

The pronounced summer rainfall peak is clearly seen in the time series of the climatological mean annual cycle (Fig. 13), which has been computed separately for land and surrounding ocean regions. Error bars pertaining to the 95% confidence limits have also been overlaid to give an indication of the magnitude of sampling error (interannual variability). The timing of the summer rainfall peak is simulated reasonably well by both models, but differences in the mean rain rate are clearly evident. WRF consistently underestimates monthly mean rainfall over land by almost

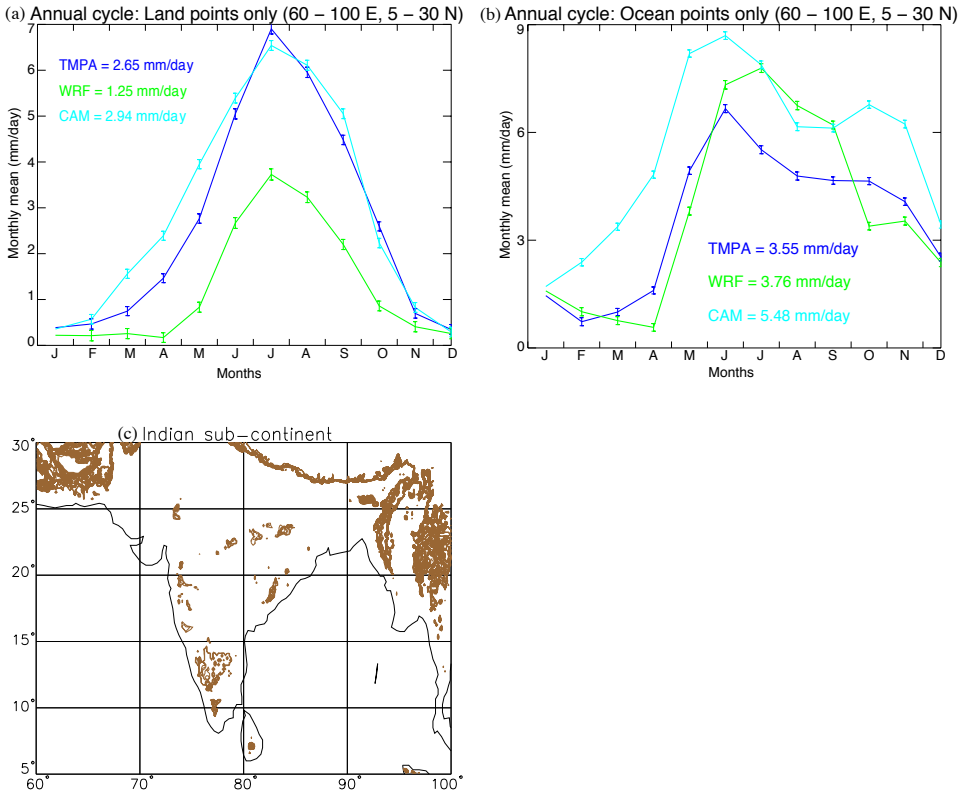

Fig. 13. Climatological mean annual cycle for Indian monsoon region (60° - 100°E, 5° - 30°N) over (a) land and (b) ocean. The annual means have been displayed for comparative purposes. The observations: TMPA are plotted in blue, WRF in green and CAM in cyan. Error bars around the monthly means have been plotted at the 95% confidence level. The last figure displays the topography over the Indian sub-continent where individual contours are drawn every 500 m.

50% compared to the observations (Fig. 13(a)). On the other hand, rainfall associated with the monsoon starts too early in CAM, while also producing a prolonged rainy season (see Fig. 13(a)). The rainfall produced by the models over the surrounding ocean region (Fig. 13(b)) has a larger variance and is indicative of the complex interaction between the SSTs, large-scale circulation and precipitation in the region (Nanjundiah et al. 2005).

The amplitude and phase of the annual harmonic (Fig. 14) shows the pro-

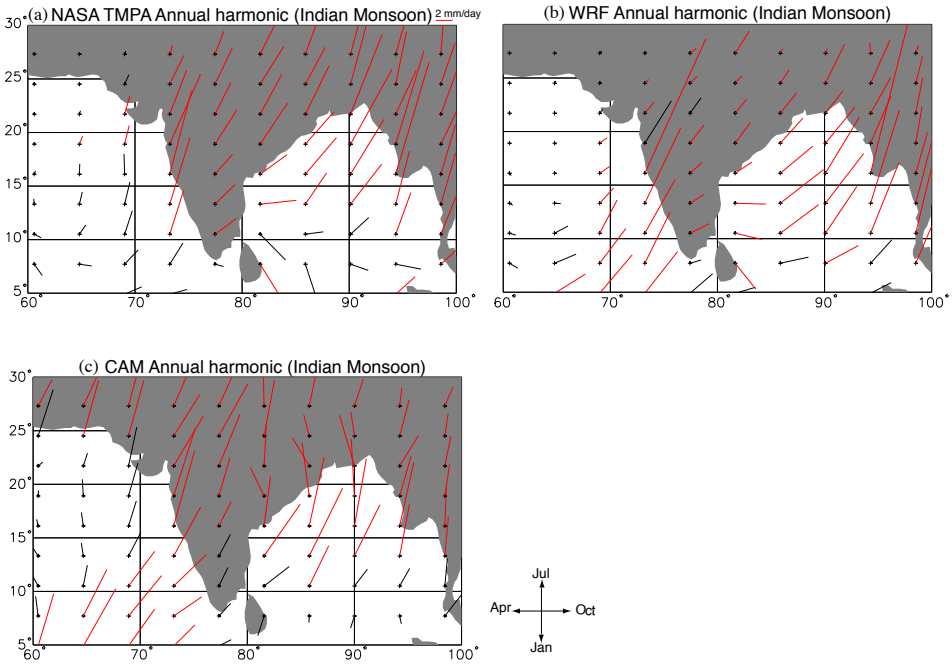

Fig. 14. Amplitude and phase of the annual harmonic for Indian monsoon region (60° - 100°E, 5° - 30°N) for (a) TMPA, (b) WRF and (c) CAM 3. The red lines indicate that the amplitude and phase are significant at the 95% confidence level. The orientation of the harmonic vectors is represented by the harmonic dial with 'January' pointing due south and 'July' due north.

gression of monsoon rainfall from the Arabian sea across the Indian sub-continent

during boreal summer. The monsoon makes landfall during mid-July (Fig. 14(a)) along the western coast of India and propagates eastward (and northward) across the continent during the next couple of months before waning in late-August/early September. These maps highlight some of the regional biases not readily evident in the averaged monthly mean time-series (Fig. 13). Overall, the models get the general progression of the monsoon right but with inconsistencies in the magnitude of rainfall simulated. WRF in particular, produces too much rainfall along the west coast and too little over land. The monsoon starts early in CAM (late-May/early-July) and is followed by a rather prolonged rainy season, consistent with our findings in Fig. 13. CAM also erroneously produces too much rainfall in April-May along the eastern coast of India which is clearly seen in the seasonal mean maps discussed below.

In order to connect the biases to circulation features, Fig. 15 displays the seasonal march of rainfall across the continent from May through October corresponding to the onset and decline of the monsoon, with 1000-850 hPa layer-averaged NCEP winds superimposed, for the observations along with the corresponding model anomalies. In WRF (Fig. 15(e)), the Western Ghats serve to block advection of rainfall by monsoon westerlies into the sub-continent leading to a pronounced maximum along the western coast and a corresponding dry bias farther inland. This feature agrees with the small amplitudes simulated by the model in Fig. 14(b). On the eastern side, the anomalous winds over the Bay of Bengal are largely westerly and consequently produce too much rainfall over Burma and southeast asia, adding to substantial dry bias over India.

In CAM, there is an anomalous low over the Arabian ocean during the pre-monsoon months (March-May, see Fig. 15(c)) that leads to convergence and moisture build-up there. The excessive moisture is transported by monsoon westerlies into the continent and leads to a wet bias over most of the sub-continent. Nanjundiah et al. (2005) attributes this wet bias to the presence of a surplus of vertically-integrated

water vapor (regulated by local SSTs) during the pre-monsoon months (May) over the Arabian sea, that causes excessive precipitation over land when advected by the westerlies. There are similarities in the seasonal rainfall distribution simulated by the models especially along the western coast of India wherein CAM also produces too much precipitation just off the coast, and too little over northeast India. The rainy season in CAM lasts well into September and October as evident in Fig. 15(i).

The divergence maps (Fig. 16) of the observations shows strong correlation between regions of heavy rainfall and large-scale convergence (negative divergence). The convergence anomalies in the models (Fig. 16(e) and (f)) are also consistent with the spatial distribution of the precipitation anomalies in Fig. 15. In particular, there appears to be a large convergence anomaly and hence moisture build-up over the Arabian ocean in CAM (Fig. 16(c)) that leads to an overestimation of monsoon rainfall during June-August. The large positive rainfall bias over the sub-continent in September-October in CAM correlates well with the large convergence that persists over the continent leading to a prolonged rainy season. Notable exceptions however include southern and central tropical Indian Ocean (IO), wherein the zone of large-scale convergence appears to have shifted north in the models and over the Himalayan plateau in WRF, wherein strong convergence coincides with a dry bias in precipitation due to lack of moisture during June-August.

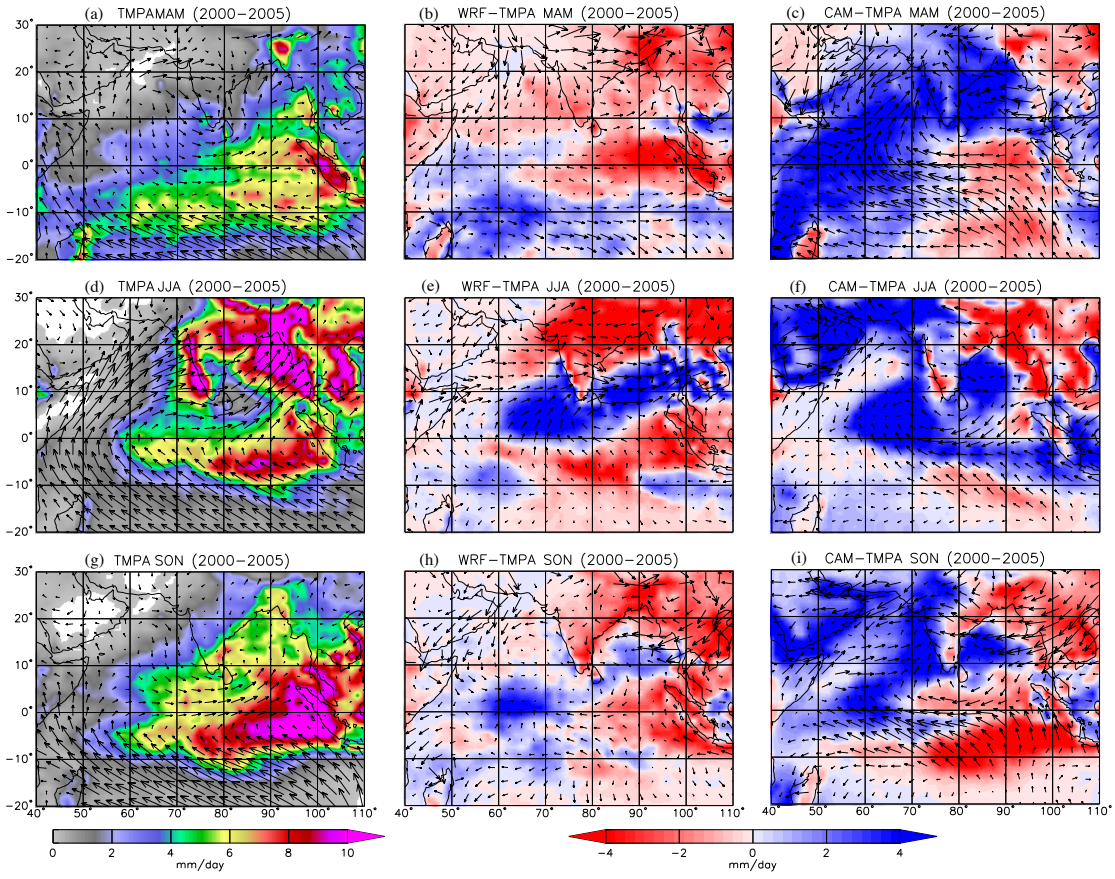

Fig. 15. Seasonal mean rainfall maps with 1000-850 hPa layer-averaged horizontal winds overlaid for (a, d, g) TMPA for March-May, June-August and September-November respectively. The departures of the model rainfall and winds from the observations ("anomalies") are also shown for (b, e, h) WRF and (c, f, i) CAM over the Indian monsoon region (60° - 100°E, 5° - 30°N) for March-May, June-August and September-November respectively.

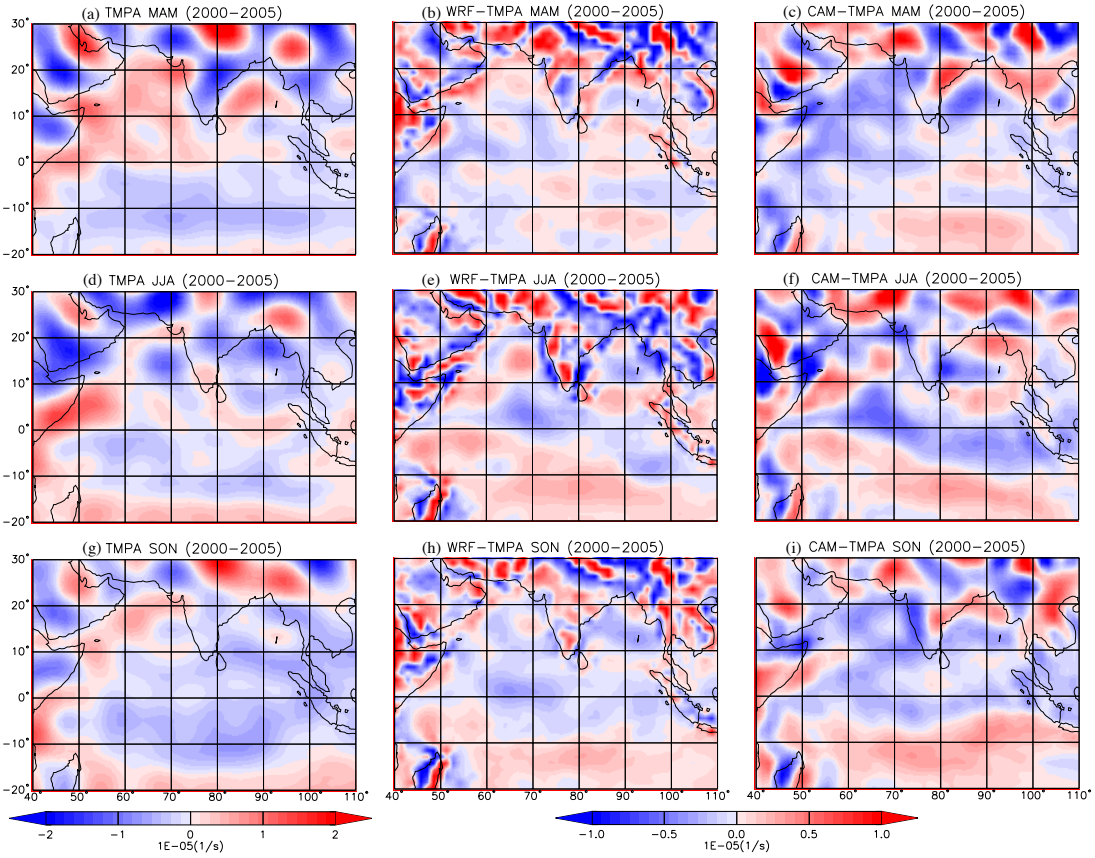

Fig. 16. Climatological mean divergence/convergence of 1000-850 hPa layer-averaged horizontal winds for (a, d, g) TMPA for March-May, June-August and September-November respectively. The departures of the model fields from the observations ("anomalies") are also shown for (b, e, h) WRF and (c, f, i) CAM over the Indian monsoon region (60° - 100°E, 5° - 30°N) for March-May, June-August and September-November respectively.

b. South America

Rainfall over the South America shows strong seasonal variability and is typically associated with large-scale features such as the ITCZ and the South-Atlantic convergence zone.. The convective activity migrates north and south following the annual march of the sun and is also forced remotely, by SSTs over both the tropical Atlantic and Pacific Oceans (Chapa and Rao 2005). The SSTs effect the location and intensity of the maritime ITCZ, which in turn influences the large-scale circulation through latent heating that extends into coastal regions causing rainfall, thereby communicating the the SST signal onshore (Biasutti et al. 2004).

Fig. 17 displays the annual cycle of rainfall over South America for regions north and south of the equator. In the south (Fig. 17(b)), a strong annual rainfall peak is observed during the austral summer (December-February) months followed by a dry season. WRF underestimates the magnitude of rainfall by almost two orders of magnitude while CAM fares marginally better. Both models get the timing of peak rainfall right south of the equator. WRF however performs better than CAM north of the equator (Fig. 17(a)), but underestimates rain particularly during the wet season. The seasonal cycle in CAM (Fig. 17(a)) bears little resemblance to the observations, consistent with the findings of Collier et al. (2004).

Comparisons between the amplitude and phase of the annual harmonic for observations and the models are displayed in Fig. 18. The northward transition of rainfall belt between the hemispheres is clearly seen in both the observations (Fig. 18(a)) and the models (Fig. 18(b) and (c)). Both models simulate the amplitude and phase of the annual cycle accurately south of the equator and produce erroneous phases in the north, in accordance with Fig. 17. Specifically, rainfall in CAM lags both WRF and the observations by a couple of months (August peak).

The seasonal mean rainfall and divergence maps for December-February and June-August (Figs. 19 and 20), help explain some of the differences observed in the Figs. 17 and 18. In December-February (Fig. 19), most of the biases are associated with the magnitude of rainfall simulated (Fig. 19(b) and (c)), although both models appear to capture the spatial patterns of monsoon precipitation reasonably well. Specifically, both WRF and CAM produce a persistent dry bias along the northeastern coast, central Amazon and southern Brazil. In WRF, there appears to be strong zone of convergence (Fig. 19(e)) associated with strong anomalous easterly winds over the Amazon basin, that surprisingly correlates with the large dry bias. We speculate that a lack of moisture in the model is the likely cause. CAM however performs better than WRF by producing smaller biases in both rainfall and horizontal winds. The large dry bias along the northeastern coast correlates well with the zone of divergence in both models (see Fig. 19(e) and (f)). WRF is able to simulate rainfall associated with topography along the Andes in the southwest, while CAM produces too much rain along the western coastline owing to the lack of representation of orography and its effect on convective processes.

In June-August, the rainfall shifts northwestward as seen in the observations (Fig. 20(a)). The divergence (convergence) patterns (Fig. 20(d)) correlate well with regions of heavy and scant rainfall. Both models produce a persistent dry bias throughout the region. This large dry bias can be attributed to the northward shifted ITCZ, that accounts for much of the rainfall in northern South America during January-August. Specifically, a local moisture deficit and weak northeasterly winds that advect rainfall inland from the ITCZ in the tropical Atlantic could lead to the reduced rainfall intensity in WRF, as most of the rainfall occurs offshore along the northeastern coast.

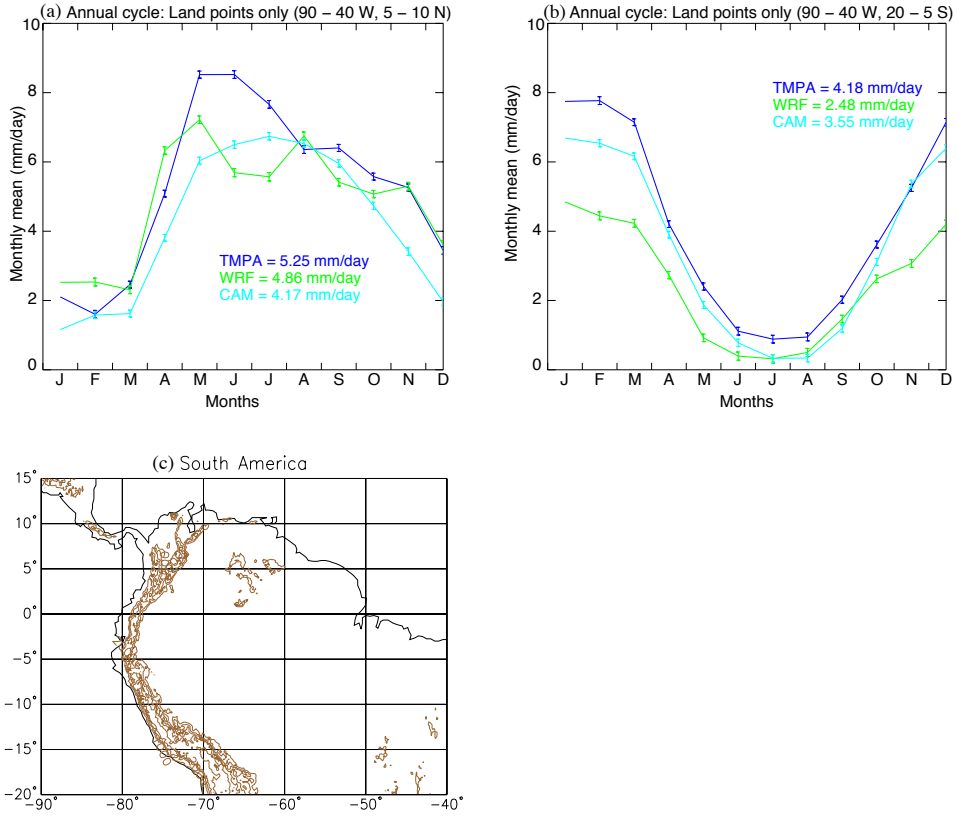

Fig. 17. Climatological mean annual cycle for South America for regions (a) north (90° - 40°W, 5° - 10°N) and (b) south (90° - 40°W, 20° - 5°S) of the equator. The annual means have been displayed for comparative purposes. The observations: TMPA are plotted in blue, WRF in green and CAM in cyan. Error bars around the monthly means have been plotted at the 95% confidence level. The last figure (c) displays the topography over South America where individual contours are drawn every 500 m.

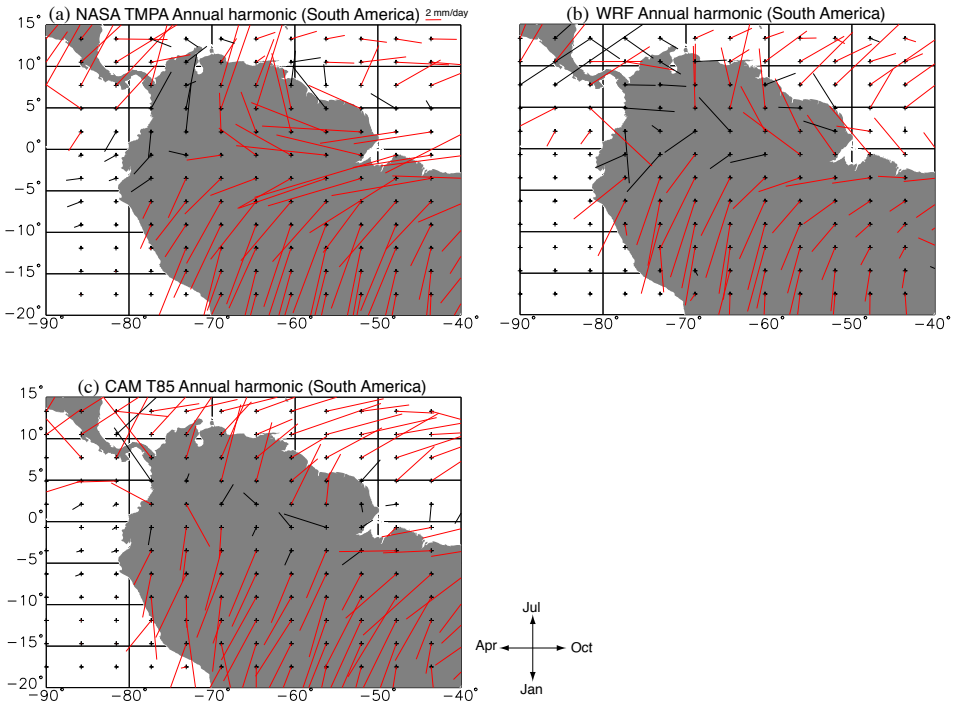

Fig. 18. Amplitude and phase of the annual harmonic for South America (90° - 40°W, 20°S - 15°N) for (a) TMPA, (b) WRF and (c) CAM. The red lines indicate that the annual harmonic is significant as the 95% confidence level. The orientation of the harmonic vectors is represented by the harmonic dial with 'January' pointing due south and 'July' due north.

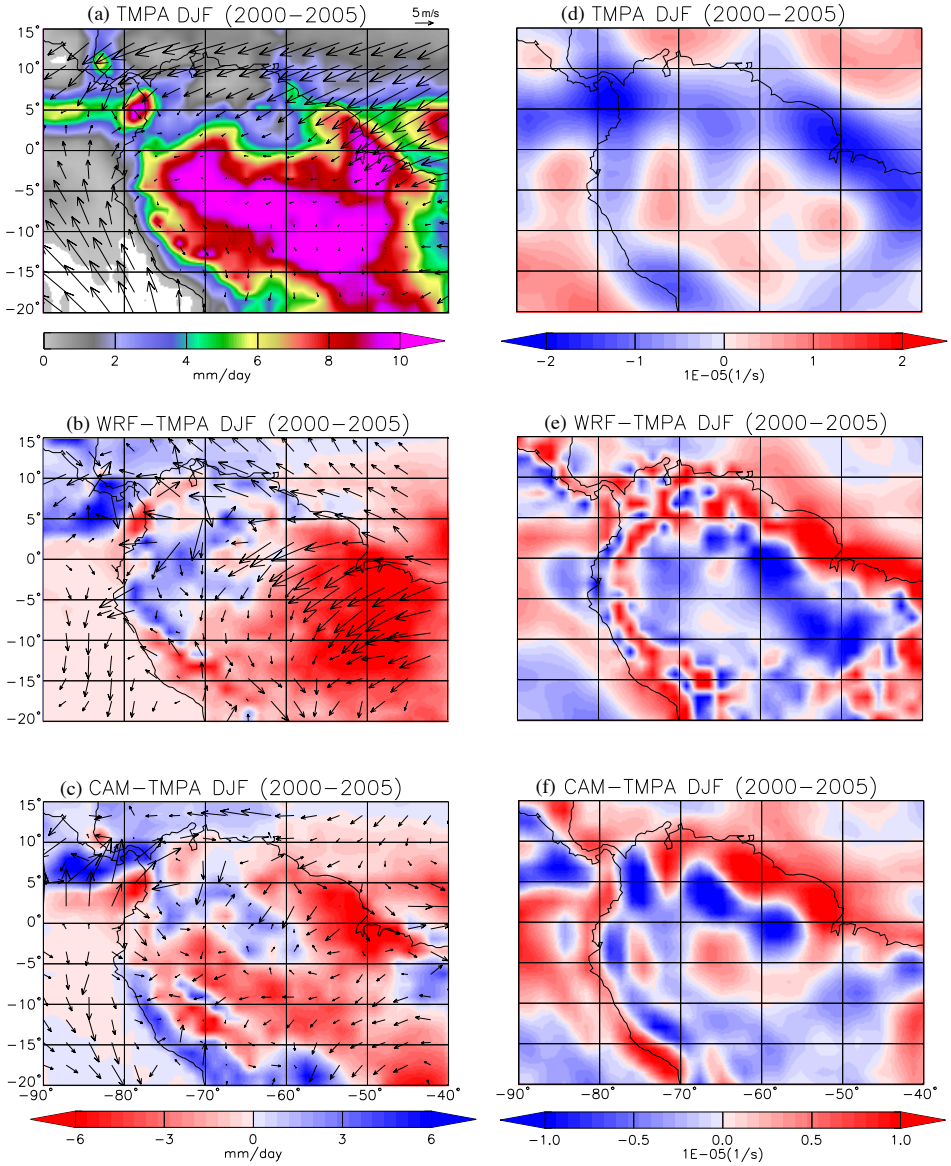

Fig. 19. Seasonal mean rainfall with 1000-850 hPa layer-averaged horizontal winds overliad for (a) TMPA. The departures of the model rainfall and winds from the observations ("anomalies") are also shown for (b) WRF and (c) CAM over South America (90° - 40°W, 20°S - 15°N) for December-February. The divergence maps of the layer-averaged winds are also shown over the region for (d) TMPA, along with the corresponding model "anomalies" for (e) WRF and (f) CAM.

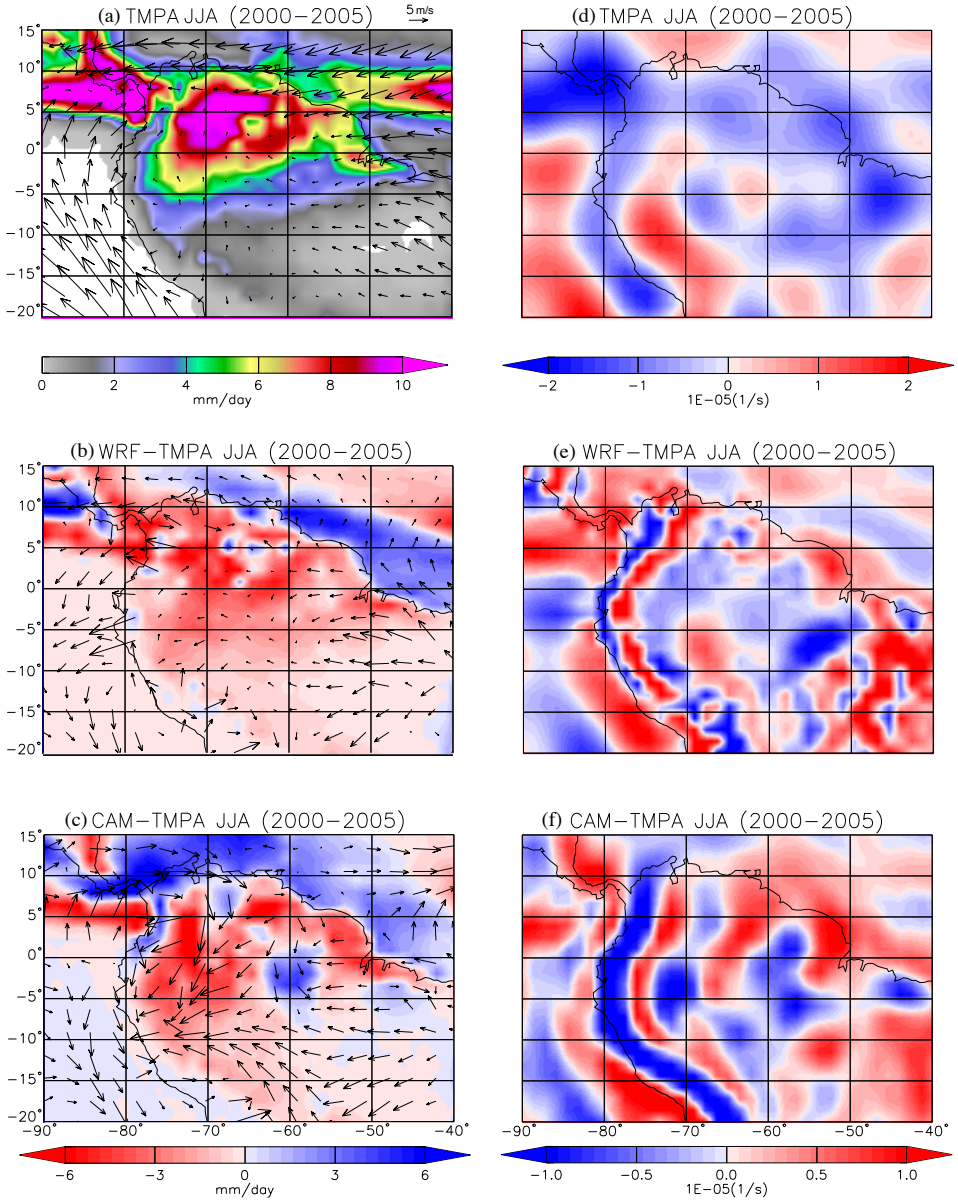

Fig. 20. Seasonal mean rainfall with 1000-850 hPa layer-averaged horizontal winds superimposed for (a) TMPA. The departures of the model rainfall and winds from the observations ("anomalies") are also shown for (b) WRF and (c) CAM over South America (90° - 40° W, 20° S - 15° N) for June-August. The divergence maps of the layer-averaged winds are also shown for (d) TMPA, along with the corresponding model "errors" for (e) WRF and (f) CAM.

c. Tropical Africa

Rainfall variability over Africa is characterized primarily by three climatic regimes namely, the equatorial, northwest and southeast monsoons (Sylla et al. 2009). The annual cycle is particularly strong in the tropical latitudes just north and south of the equator, and primarily follows the seasonal march of the sun across the globe (Nicholson 2000; Jury and Mpeta 2005).

A strong July-August peak in rainfall is seen in the northern hemisphere

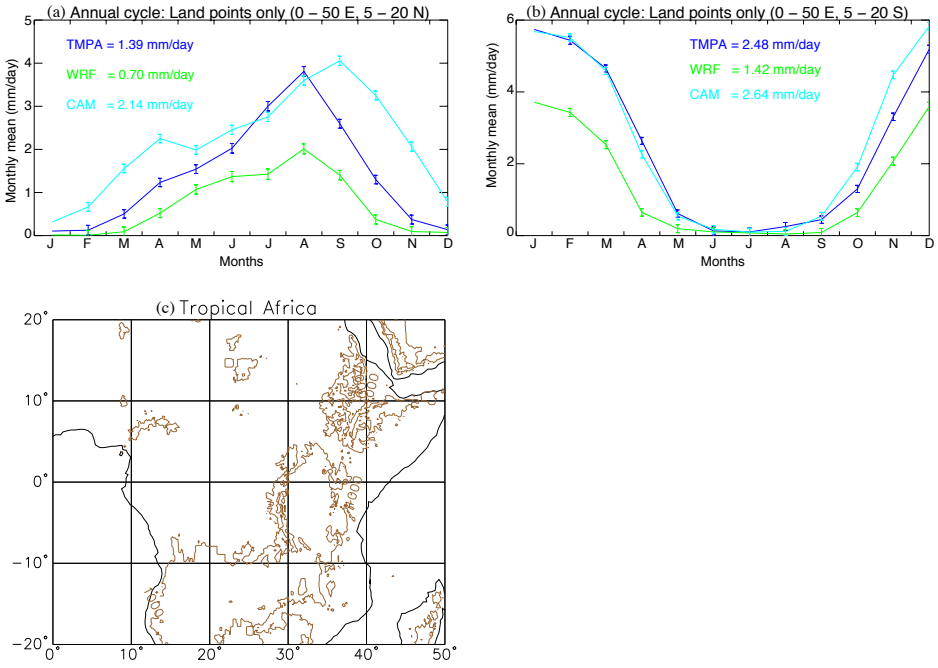

Fig. 21. Climatological mean annual cycle over tropical Africa for regions (a) north (0° - 50°E, 5° - 20°N) and (b) south (0° - 50°E, 20° - 5° S) of the equator. The annual means have been displayed for comparative purposes. TMPA is plotted in blue, WRF in green and CAM in cyan. Error bars around the monthly means have been plotted at the 95% confidence level. The last figure (c) displays the topography over tropical Africa where individual contours are drawn every 500 m.

between latitudes of about 5°and 20° N (Fig. 21(a)). WRF is able to reproduce the timing of the peak rainfall, but consistently underestimates the magnitude throughout the year. The rainfall in CAM lags the August peak by a month and consistently over-predicts the monthly means throughout the rainy season. South of the equator (Fig. 21(b)), a similar trend is observed but CAM performs better than WRF when compared to the observations. Here again, WRF systematically under-predicts the rainfall by about 50%, but both models capture the dry season accurately.

The harmonic vector maps (Fig. 22) confirm the general trends observed in Fig. 21. Both models get the phase of the annual cycle right throughout tropical Africa with noticeable differences in the amplitude of rainfall. The northward extent of the January-August rainfall band is smaller in WRF (Fig. 22(b)) and it systematically underestimates rainfall in the region. In CAM, the northern hemispheric summer rainfall belt seems to have shifted north but it produces amplitudes that are comparable to the observations, in general agreement with Fig. 21. The delayed rainfall peak in CAM (mid-August to early September), is particularly visible in the northeast over the Sudan and the Ethiopian highlands (see Fig. 22(c)). The equatorial regime has a significant semi-annual cycle with a primary maximum occurring in April-June and a secondary one in September-October (not shown). Both models are able to reproduce this feature accurately but produce smaller rain rates.

The spatial pattern of seasonal precipitation and divergence/convergence over Africa are displayed separately for December-February (Fig. 23) and June-August (Fig. 24) along with the corresponding model anomalies. In general, the patterns of divergence/convergence in either hemisphere agree well with the seasonal march of the major rainfall bands across the equator. In WRF, the highlands in the east obstruct the moist north-easterlies from the IO and produce a precipitation maximum along the eastern coast, leaving most of the interior dry in December-February (Fig. 23(b)).

On the western side, the anomalous winds are predominantly dry northwesterlies that contribute towards a rainfall deficit in the region. The divergence maps (Fig. 23(e)) also displays a rather substantial area of convergence in central-western equatorial Africa that correlates with a dry bias in precipitation due to drier northwesterly flow and lack of moisture in the model. CAM also produces the same dry bias over the equatorial west coast, but produces too much rain everywhere else including regions north of the equator. The reasons for this large dry bias are not clearly evident, but we speculate that it has to do with the representation of land-atmosphere interaction processes in the model.

In January-August (Fig. 24(a)), the ITCZ lies far north of the equator between 18° and 20° N and accordingly the west African monsoon rainfall is at its maximum. Both models reproduce the low-level circulation fairly well. However, WRF underestimates rainfall by about 2 mm/day throughout northern tropical Africa and could once again be attributed to a lack of moisture in the model (Fig. 24(b) and (e)). WRF however produces isolated rainfall peaks associated with local orography (large maximum over Ethiopian highlands), that is not seen CAM owing to its lower resolution. CAM on the other hand produces a large wet bias almost everywhere north of the equator in January-August, except along the Guinea coast and Ethiopian highlands where like WRF, it underestimates seasonal rainfall (Fig. 24(c)).

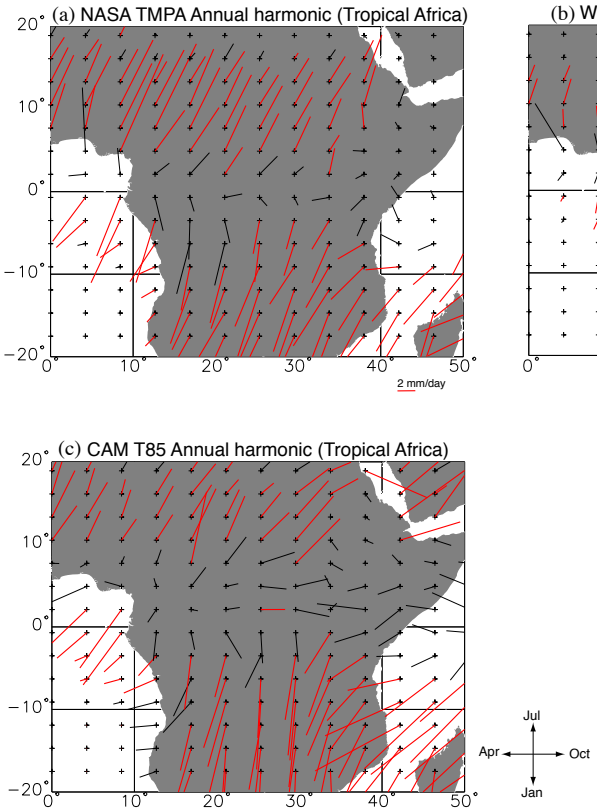

Fig. 22. Amplitude and phase of the annual harmonic for tropical Africa (0° - 50°E, 20°S - 20°N) for (a) TMPA, (b) WRF and (c) CAM. The red lines indicate that the annual harmonic is significant as the 95% confidence level. The orientation of the harmonic vectors is represented by the harmonic dial with 'January' pointing due south and 'July' due north.

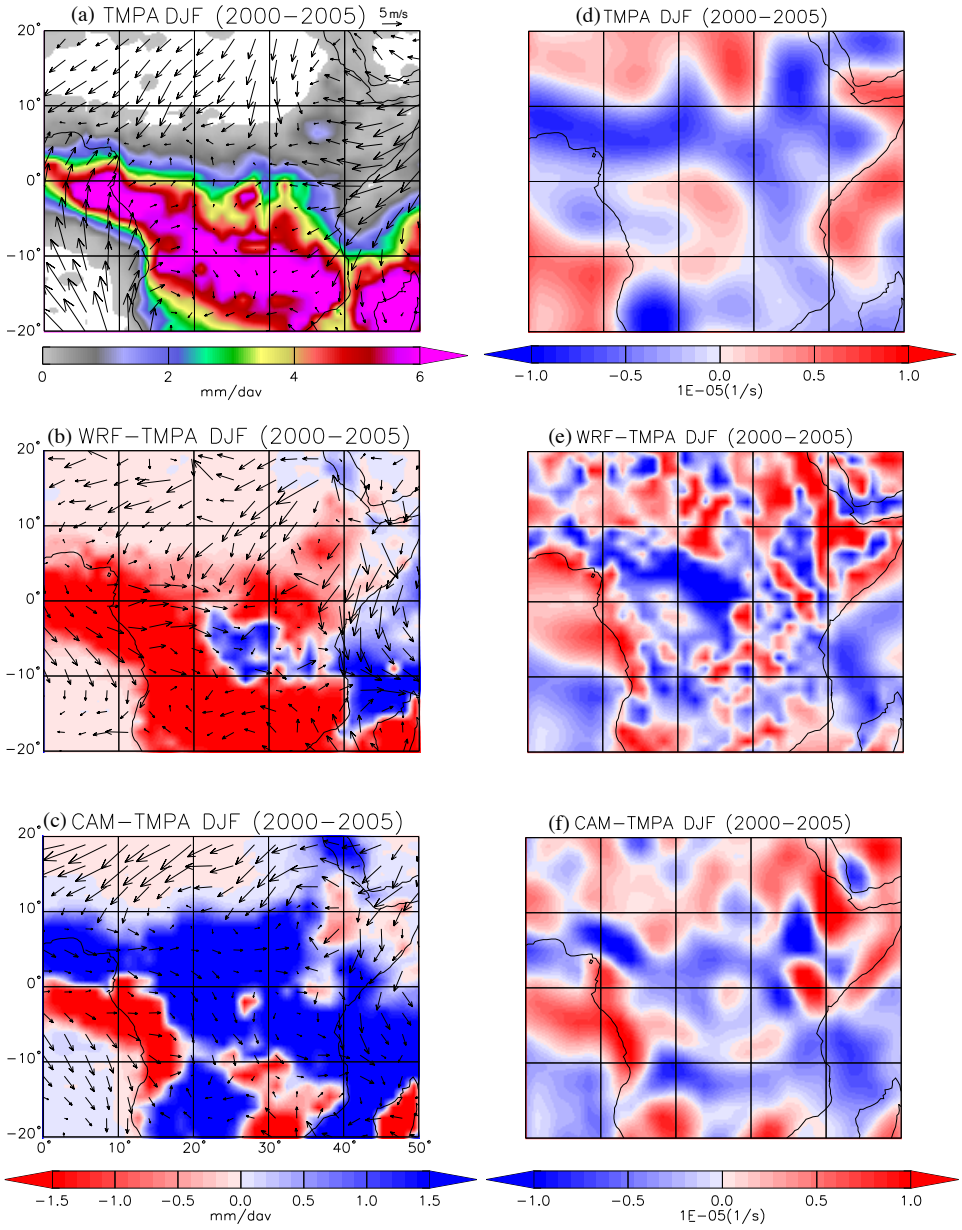

Fig. 23. Seasonal mean rainfall with 1000-850 hPa layer-averaged horizontal windsoverliad for (a) TMPA. The departures of the model rainfall and winds from the observations ("anomalies") are also shown for (b) WRF and (c) CAM over tropical Africa (0° -50°E, 20°S - 20°N) for December-February. The divergence maps of the layer-averaged winds are also shown over the region for (d) TMPA, along with the corresponding model "anomalies" for (e) WRF and (f) CAM.

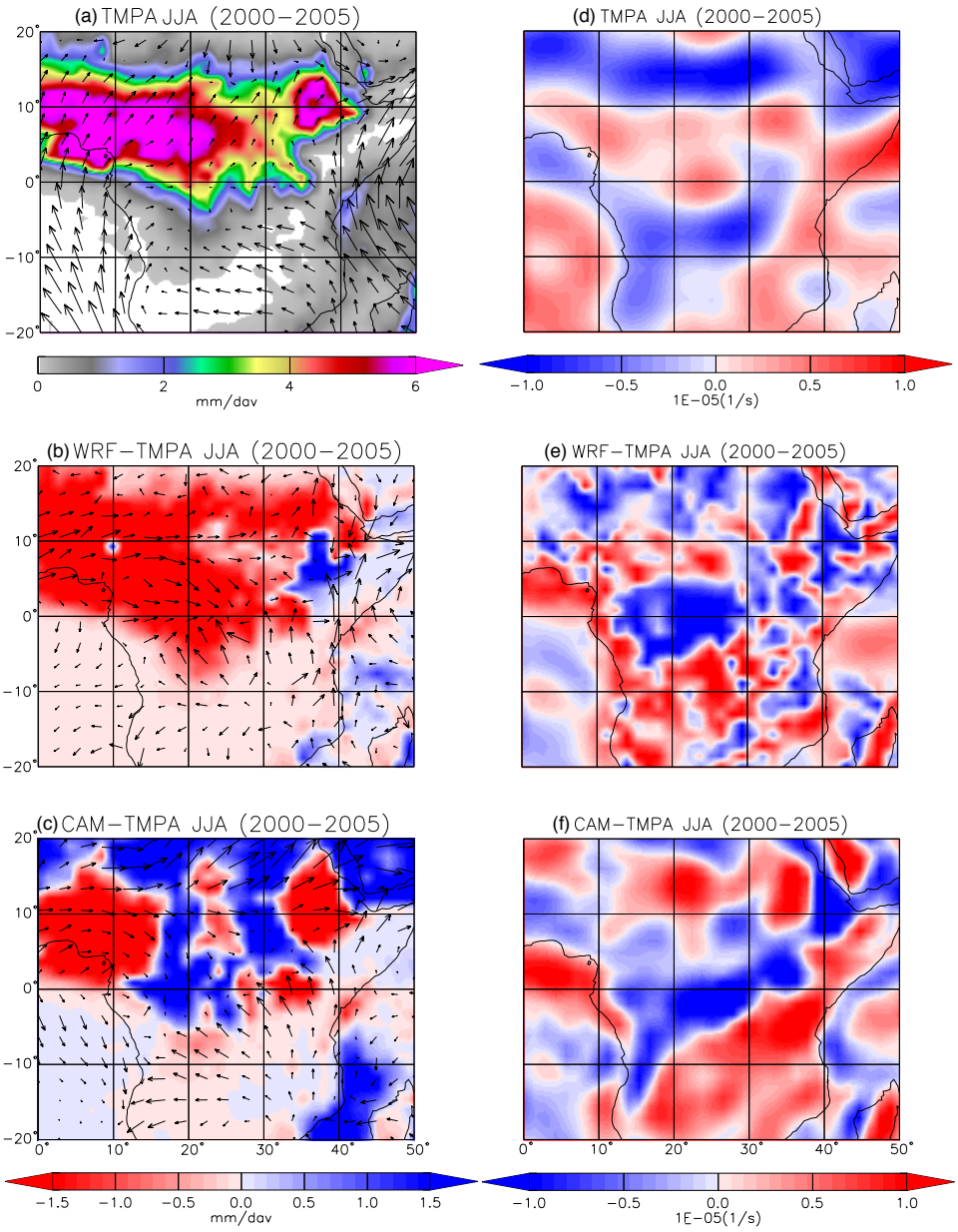

Fig. 24. Seasonal mean rainfall with 1000-850 hPa layer-averaged horizontal winds overliad for (a) TMPA. The departures of the model rainfall and winds from the observations ("anomalies") are also shown for (b) WRF and (c) CAM over tropical Africa (0° -50°E, 20°S - 20°N) for June-August. The divergence maps of the layer-averaged winds are also shown over the region for (d) TMPA, along with the corresponding model "anomalies" for (e) WRF and (f) CAM.

d. North American monsoon (NAM) region

Higgins et al. 1997 describe the evolution of the North American Monsoon System (NAMS) as being characterized by three phases: development, mature and decay. The rainfall system develops during May-June, increases in intensity during July producing heavy rainfall over large-areas of the southwestern United States and northwestern Mexico, before finally waning in mid-September (Adams and Comrie 1997). The onset of the monsoon over southwestern Mexico is characterized by heavy rainfall in the region that quickly spreads northward along the western slopes of the Sierra Madre Occidental (SMO) and into Arizona and New Mexico by early July. See Badan-Dagan et al. (1991), Carleton (1986, 1987) and Okabe (1995).

The time-series of the annual cycle for the NAM region (Fig. 25) indicates that neither model does very well in their simulation of monthly mean rainfall by producing substantial dry biases. CAM simulates an early onset of the monsoon in May and also shuts off a month earlier (August). Conversely, WRF gets the timing of the monsoon right but produces smaller rain rates during July. The rainfall however recovers during August-September and wanes thereafter, a trend that is similar to the observations. The harmonic vector maps (Fig. 26) reinforce the main points discussed above wherein the early rainfall peak produced by CAM is clearly seen over central and eastern Mexico.

Fig. 27 shows the mean precipitation and divergence/convergence anomaly maps for January-August. The continuous stream of northward flow associated with monsoon westerlies is seen in the observations (Fig. 27(a)) over western Mexico and the Gulf of California (GoC). The models appear to be generating a strong northwesterly (i.e directed from the northwest to the southeast along the GC) flow which inhibits northward advection of moisture leading to a substantial dry bias along the northern

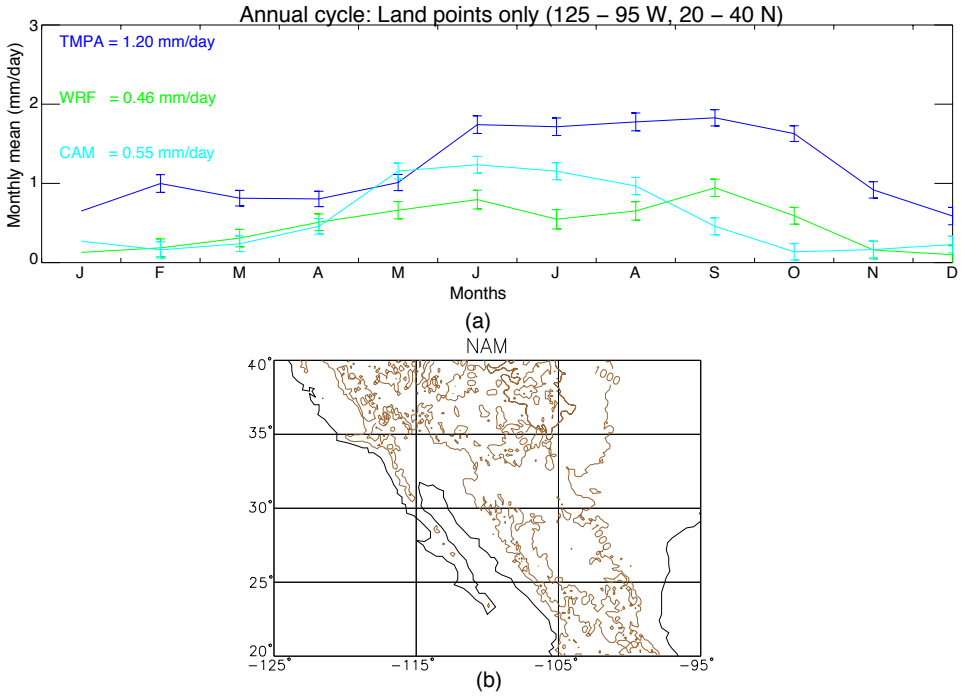

Fig. 25. Climatological mean annual cycle for (a) the North American monsoon (NAM) region (125° - 95°W, 20° - 40°N) and (b) topography of the NAM region, where individual contours are drawn every 500 m. The annual means have been displayed for comparative purposes. The observations: TMPA are displayed in blue, WRF in green and CAM in cyan. Error bars around the monthly means have been plotted at the 95% confidence level.

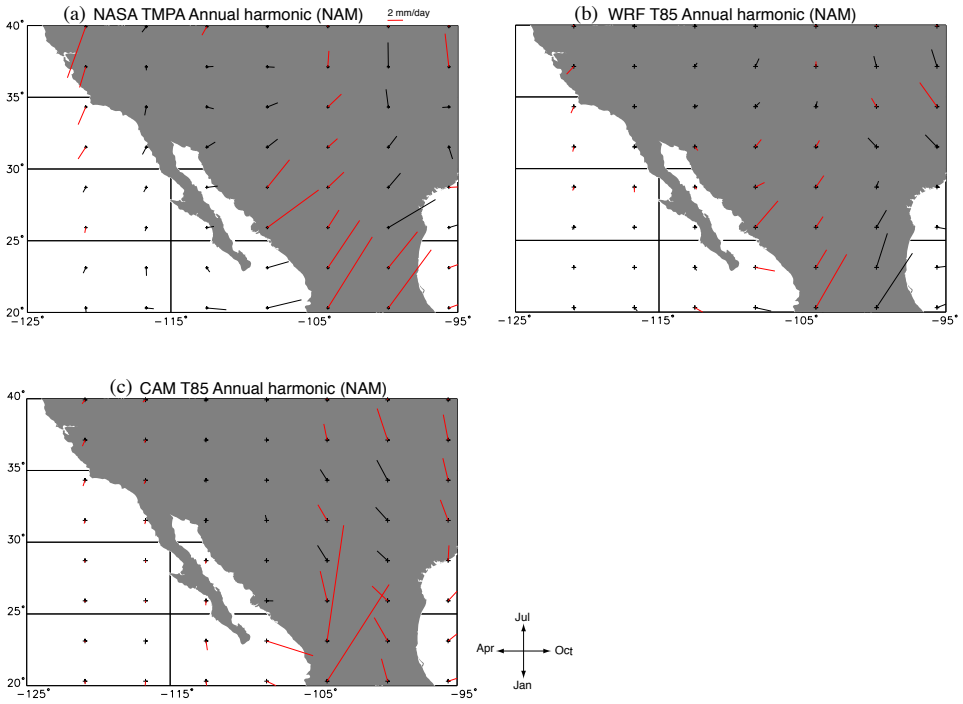

Fig. 26. Amplitude and phase of the annual harmonic for the North American monsoon (NAM) region (125° - 95°W, 20° - 40°N) for (a) TMPA, (b) WRF and (c) CAM. The red lines indicate that the annual harmonic is significant as the 95% confidence level. The orientation of the harmonic vectors is represented by the harmonic dial with 'January' pointing due south and 'July' due north.

flank of NAM. In WRF, the dry bias over southwestern Mexico and the GoC is attributed in part to the large divergence (Fig. 27(e)) associated with flow offshore that impedes transport of moisture from the SMO and GoC towards the northwest. CAM however, produces excessive precipitation over the SMO and southwestern Mexico but produces rainfall patterns similar to WRF everywhere else.

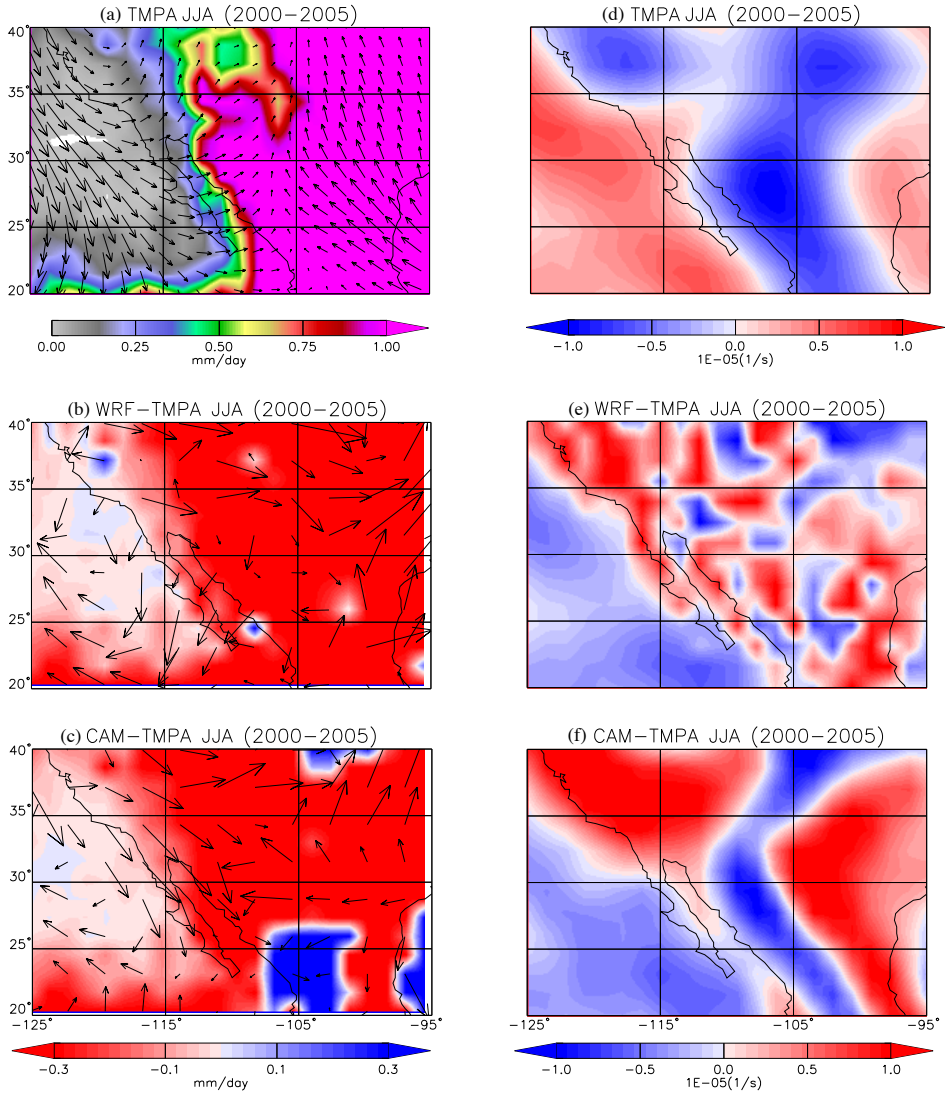

Fig. 27. Seasonal mean rainfall with 1000-850 hPa layer-averaged horizontal winds overliad for (a) TMPA. The departures of the model rainfall and winds from the observations ("anomalies") are also shown for (b) WRF and (c) CAM over the North American monsoon (NAM) region (125° - 95°W, 20° - 40°N). The divergence maps of the layer-averaged winds are also shown over the region for (d) TMPA, along with the corresponding model "anomalies" for (e) WRF and (f) CAM.

E. Summary and conclusions

One of the goals of this study was to ascertain whether the use of higher spatial resolution (36-km) capable of resolving mesoscale features in the least, led to an improvement in the simulation of seasonal rainfall. Our main inferences are summarized below. Substantial biases (compared to the observations) are evident in the long-term time means for both models. WRF systematically underestimates the magnitude of mean rainfall over most land regions while the biases in CAM depend on the region being studied. Both models produce a substantial wet bias in the western Pacific warm pool south of the equator, while generally simulating the ITCZ correctly over the western and portions of the central Pacific. However, the ITCZ over the eastern Pacific is displaced a few degrees north in both models, and leads to a reduction in monsoon rainfall over South America.

CAM produces a significantly wet bias over the Indian sub-continent during summer that lasts well into late-September/early-October. The presence of an anomalous low over the Arabian sea during May is diagnosed as the likely cause for the wet bias. WRF produces a uniform dry bias over land, while both models produce excessive rainfall just off the west coast of India leaving the interior dry. This could imply that the influence of orography on advection of moisture into the continent is significant, but one would need to examine vertical profiles of moisture to make definitive conclusions. In regions south of the equator over South America, both WRF and CAM reproduce the timing of peak rainfall that agrees well with the observations, but underestimate the magnitude of mean rainfall. CAM does poorly over northern South America in its simulation of the annual cycle by producing smaller rainfall magnitudes that last well beyond the boreal summer season. By contrast, WRF produces a peak in April-May (early onset) after which the monsoon weakens thereby

under-predicting rainfall on average.

Over tropical Africa, the phase of the annual cycle is simulated fairly well by both models in January-August and December-February, although in CAM (January-August) the monsoon starts early and extends well into the winter months. WRF significantly underestimates rainfall during both hemispheric summer seasons. This can be attributed to the strong influence of orography on moisture advection from adjacent oceans into the continent and weaker low-level flow. The general trend observed in other tropical regions described in this study is also prevalent in the North American Monsoon region. WRF under-predicts rainfall amount compared to the observations (and CAM). In particular, the anomalous northwesterly winds flowing down the GoC, tends to obstruct northward transport of moisture from the SMO and GoC regions into the northwestern United States causing a dry bias in the region in both models.

Overall, simulation of the annual cycle by both models suffer from systematic biases over most of the global Tropics compared to the observations. The improved resolution in WRF (36-km) does not seem to better simulate precipitation and conversely produces too little rainfall over most of the tropical land regions compared to CAM, except in small regions forced by local orography. However, WRF simulates the seasonal timing of rainfall better than CAM. Alternatively, CAM reproduces the magnitudes of mean rainfall fairly well, but the rainfall leads or lags the observations by a month or so over most regions.

CHAPTER IV

CONCLUSIONS

A. Summary

The variability of precipitation is a very important subject because of its influence on and response to the atmospheric and surface water-energy cycles, which strongly govern weather and climate. Precipitation variability spans a wide range of scales, from local-diurnal scales down to global-decadal and longer scales. Quantifying this spatio-temporal variability by using satellite-derived rainfall products and comparisons with a variety of statistical and climate models forms the crux of this study.

In order to ascertain whether a space-time relationship exists for precipitation fields, we test the validity of the Taylor "frozen field" hypothesis (TH) that is commonly applied to turbulent flows to infer the spatial description of the flow properties from temporal information at a single point in the flow field. In this regard, we test the TH applied to the space-time covariance function of the rainfall field (radar reflectivities) i.e. we test whether the temporal covariance at a given spatial location is equal to the corresponding spatial covariance scaled by the mean flow velocity at a given time instant. Note that the hypothesis assumes a stationary covariance field in both space and time and a uniform flow velocity, both of which are violated in the case of rainfall fields. The TH applied to rainfall has been studied by several researchers who concluded that it held for time scales up to about 30-40 minutes and spatial scales of around 20 km (See Zawadski 1973; Gupta and Waymire 1987; Crane 1990 and Poveda and Zuluaga 2005). In this study we use a rigorous statistical approach to test the TH based on the asymptotic joint normality of covariance estimators and compare the same with simple-minded estimates of statistical significance based on

the assumption of independence of the covariance estimates. The method is applied to high-resolution gridded NEXRAD radar reflectivity data.

The results indicate that the TH hold for only one out of the sixteen tests cases and moreover does not hold for fields characterized by advection, diffusion and decay as described the analytical model in chapter IID. However, there is a strong possibility that the TH might hold for shorter spatial and temporal scales than what is resolved by the data (4 km and 15 minutes). The simple t-test tends to overestimate the significance of the difference between correlation estimates by not accounting for the correlation between those estimates as is indicated by smaller p-values compared to those obtained by the hypothesis testing procedure in chapter IIC.

The ability of climate models to simulate the seasonal variability of rainfall is addressed by comparing long-time simulations of precipitation from the Weather Research and Forecast (WRF) model and the Community Atmosphere Model (CAM) with satellite observations. Comparisons between the model and observations are made by simulating long-term means and a physically forced component of rainfall variability such as the annual cycle. The results are presented in terms of maps of long-term mean rain rates, amplitude and phase of the annual cycle, seasonal mean rainfall and difference (model minus observations) maps. We try to quantify the biases that arise between the models and observations by closely examining the patterns in the large-scale circulation, namely the horizontal wind and divergence fields.

The main objective here is to determine whether the 36-km high-resolution (WRF) tropical channel model is better able to simulate seasonal rainfall variability by resolving mesoscale features as compared to CAM. The results indicate that substantial biases are produced by the models in their simulation of both the long-term means and the annual cycle. WRF systematically underestimates monthly mean rainfall by about 50% over most Tropical land regions, but gets the timing of the rainfall

right. CAM produces rainfall magnitudes that are comparable to the observations, but the peak rainfall leads or lags the observations (and WRF) by a few months. We conclude that the improved resolution in WRF (36-km) does not in general, lead to better simulations of precipitation. WRF produces too little rainfall over most of the Tropical land regions, except in small regions forced by local orography.

1. Recommendations for future work

The substantial underestimates of precipitation produced by WRF over most land regions could be caused by problems with evapotranspiration (ET) and hence "moisture recycling" in the land-surface component (LSM) of the model. Moisture recycling is defined as the fraction of precipitation that comes from local evaporation, as opposed to transport by horizontal advection, that contributes to precipitation over a region (Trenberth 1997). Koster et al. (2004) performed extensive AGCM simulations to ascertain regions of the globe where land-atmosphere coupling via soil moisture (i.e. moisture recycling) significantly impacts seasonal precipitation variability. They concluded that almost 25 - 40 % of the precipitation over regions such as Tropical Africa, central and southern Mexico and the Amazon, comes from local evaporation during the monsoon months. However, moisture recycling is essentially a feedback process, and if the LSM produces a negative bias in ET, this would produce a dry bias in precipitation, that would further reduce ET. To compare the strength of moisture recycling between WRF and CAM, one could examine the evaporative fraction, a useful proxy for land-atmosphere interactions (Betts 2004) defined as the ratio of the latent heat flux to the total (latent plus sensible) heat flux, to determine if major differences exist between the role of land-atmosphere interactions on precipitation in the two models. We therefore intend carrying out a series of simulations, to understand the role of ET in producing the observed differences between the models and

the satellite observations.

In addition to the above, one would also need to test the various cumulus convective and land-surface parameterizations in the models to identify potential errors arising from representation of physical processes themselves, since it is difficult to attribute causality to a single factor. The next step in our analysis would thus involve conducting more extensive experiments with the WRF model, using a variety of "cloud-resolving" spatial resolutions (12, 10, 4, 2 km) with variable convection and land-surface parameterization schemes over a specific region. We hope that the high resolution data obtained from these experiments will help distinguish the dynamical downscaling ability of the model from the inherent parameterization and hence lead to a better understanding of model generated precipitation.

REFERENCES

Adams, D. K., and A. C. Comrie, 1997: The North American monsoon. *Bull. Amer. Meteor. Soc.,* **78**, 2197—2213.

Adler, R. F., G. J. Huffman, D. T. Bolvin, S. Curtis, and E. J. Nelkin, 2000: Tropical rainfall distributions determined using TRMM combined with other satellite and rain gauge information. *J. Appl. Meteor.,* **39**, 2007—2023.

Anderson, T. W., 1971: *The Statistical Analysis of Time Series*, 704 pp, John Wiley.

Barnett, T. P., 1995: Monte Carlo climate forecasting. *J. Climate.,* **8**, 1005—1022.

Bell, T. L., A. Abdullah, R. L. Martin, and G. R. North, 1990: Sampling errors for satellite-derived tropical rainfall: Monte Carlo study using a space-time stochastic model. *J. Geophys. Res.,* **95D**, 2195—2205.

—, and P. K. Kundu, 1996: A study of the sampling error in satellite rainfall estiamtes using optimal averagaing of data and a stochastic method. *J. Climate*, **9**, 1251-1268.

—, and —, 2000: Dependence of satellite sampling error on monthly averaged rain rates: Comparison of simple models and recent studies. *J. Climate,* **13**, 449—462.

—, —, and C. D. Kummerow, 2001: Sampling errors of SSM/I and TRMM rainfall averages: Comparison with error estimates from surface data and a simple model. *J. Appl. Meteor.,* **40**, 938—954.

Betts, A. K., 2004: Understanding hydrometeorology using global models. *Bull. Amer. Meteor. Soc.,* **85**, 1673—1688, doi:10.1175/BAMS-85-11-1673.

Biasutti, M., D. S. Battisti and E. S. Sarachik, 2003: The annual cycle over the tropical Atlantic, South America and Africa. *J. Climate,* **16**, 2491—2508.

—, — and —, 2004: Mechanisms controlling the annual cycle of precipitation in the tropical Atlantic sector in an atmospheric GCM. *J. Climate,* **17**, 4708—4723.

Bowman, K. P., A. B. Phillips and G. R. North, 2003: Comparison of TRMM rainfall retrievals with rain gauge data from the TAO/TRITON buoy array. *Geophys. Res. Lett.,* **30**, 175, doi:10.1029/2003GL017552.

—, 2004: Comparison of TRMM precipitation retrievals with rain gauge data from ocean buoys. *J. Climate,* **18**, 178—190.

Boyle, J. S., 1998: Evaluation of the annual cycle of precipitation over the United States in GCMs: AMIP simulations. *J. Climate,* **11**, 1041—1055.

Browning, K. A., 1990: Rain, rainclouds and climate. *Quart. J. Roy. Meteor. Soc.,* **116**, 1025—1051.

Burghelea, T., E. Serge, and V. Steinberg, 2005: Validity of the Taylor hypothesis in a random spatially smooth flow. *Phys. of Fluids*, **17**, 1-8.

Cahalan, R. F., D. A. Short, and G. R. North, 1981: Cloud fluctuation statistics. *Monthly Weather Review*, **110**, 26—43.

Carleton, A. M., 1986: Synoptic-dynamic character of "bursts" and "breaks" in the southwest U. S. summer precipitation singularity. *J. Climatol.,* **6**, 605—623.

—, 1987: Summer circulation climate of the American Southwest 1945—1984. *Ann. Assoc. Amer. Geogr.,* **77**, 619—634.

Carlstein, E., 1986: The use of subseries values for estimating the variance of a general statistic from a stationary sequence. *Ann. Stat.,* **14**, 1171-1179.

Chapa, S. R., and V. B. Rao, 2005: Annual cycle of precipitation and moisture characteristics over Brazil. Available at http://mtc-m15.sid.inpe.br/col/cptec.inpe.br/walmeida/2004/10.14.16.44/doc/SrinivasaAnnual%20cycle%20precipitation.eps.

Collier, J. C., K. P. Bowman, and G. R. North, 2004: A comparison of tropical precipitation simulated by the Community Climate Model (CCM3) with that measured by the Tropical Rainfall Measuring Mission (TRMM) satellite. *J. Climate,* **17**, 3319—3333, doi: 10.1175/1520-0442(2004)017¡3319:ACOTPS¿2.0.CO 2.

Collins, W. D., C. M. Bitz, M. L. Blackmon, G. B. Bonan, C. S. Bretherton, J. A. Carton, P. Chang, S. C. Doney, J. J. Hack, T. B. Henderson, J. T. Kiehl, W. G. Large, D. S. McKenna, B. D. Santer and R. D. Smith, 2006: The Community Climate System Model: CCSM3. *J. Climate,* **19**, 2122—2143.

Cox, D. R., and V. Isham, 1988: A simple spatial-temporal model of rainfall. *Proc. Roy. Soc. London Ser. A*, **415**, 317—328.

Crane, R. K., 1990: Space-time structure of rain rate fields. *J. Geophys. Res.*, **95**, 2011—2020.

Fu, R., R. E. Dickinson, M. Chen and H. Wang, 2001: How do tropical sea surface temperatures influence the seasonal distribution of precipitation in the equatorial Amazon? *J. Climate,* **14**, 4003— 4026.

Gadgil, S., and S. Sajani, 1998: Monsoon precipitation in AMIP runs. *Climate Dyn.,* **14**, 659—689.

—, 2003: The Indian monsoon and its variability. *Ann. Rev. Earth Planet. Sci.,* **31**, 429—467.

Gneiting, T., M. G. Genton, and P. Guttorp, 2007: Geostatistical space-time models, stationarity, separability and full symmetry, in Finkenstaedt, B., Held, L. and Isham, V. (eds.), *Statistics of Spatio-Temporal Systems*, Chapman & Hall/CRC Press, Monographs in Statistics and Applied Probability, 151—175.

Goswami, B. N., W. Guoxiong and T. Yasunari, 2005: The annual cyle, intraseasonal oscillations and roadblock to seasonal predictability of the Asian summer monsoon. *J. Climate,* **19**, 5078—5099.

Gupta, V. K., and E. Waymire, 1987: On Taylor's hypothesis and dissipation in rainfall. *J. Geophys. Res.*, **92**, 9657—9660.

Higgins, R. W., Y. Yao and X. L. Wang, 1997: Influence of the North American monsoon system on the U.S. summer precipitation regime. *J. Climate,* **10**, 2600—2622.

Hong, S-Y., J. Dudhia, and S-H. Chen, 2004 A revised approach to ice microphysical processes for the bulk parameterization of clouds and precipitation. *Mon. Wea. Rev.,* **132**, 103—120.

—, Y. Noh, and J. Dudhia, 2006: A new diffusion package with an explicit treatment of entrainment processes. *Mon. Wea. Rev.,* **134**, 2318—2341.

Huffman, G., and D. T. Bolvin, 2008: TRMM and other precipitation data sets documentation. Technical Report. Laboratory of Atmospheres, NASA Goddard Space Flight Center and Science Systems Applications Inc. Greenbelt, MD.

Jury, M. R., and E. J. Mpeta, 2005: The annual cycle of African climate and its variability. *Water SA,* **31**, 1—8.

Kalnay, E., M. Kanamitsu, R. Kistler, W. Collins, D. Deaven, L. Gandin, M. Iredell, S. Saha, G. White, J. Woollen, Y. Zhu, A. Leetmaa, R. Reynolds, M. Chelliah, W. Ebisuzaki, W. Higgins, J. Janowiak, K.C. Mo, C. Ropelewski, J. Wang, R. Jenne, and D. Joseph, 1996: The NCEP/NCAR 40-year reanalysis project. *Bull. Amer. Meteor. Soc.*, **77**, 437—471.

Kiehl, J., J. Hack, G. Bonan, B. Boville, B. Briegleb, D. Williamson and P. Rasch, 1996: Description of the NCAR Community Climate Model (CCM3). Technical Report NCAR/TN-420+STR, NCAR, National Center for Atmospheric Research, Boulder, CO.

Koster, R. D., P. A. Dirmeyer, Z. Guo, G. Bonan, E. Chan, P. Cox, C. T. Gordon, S. Kanae, G. Kowalczyk, D. Lawerence, P. Liu, C-H Lu, S. Malyshev, B. McAvaney, K. Mitchell, D. Mocko, T. Oki, K. Oleson, A. Pitman, Y. C. Sud, C. M.Taylor, D. Verseghy, R. Vasic, Y. Xue and T. Yamada, 2004: Regions of strong coupling between soil moisture and precipitation. *Science,* **305**, 1138—1140.

Kummerow, C., W. Barnes, T. Kozu, J. Shue and J. Simpson, 1998: The tropical rainfall measuring mission sensor package. *J. Atmos. Ocean. Tech.,* **15**, 809—817.

—, J. Simpson, O. Thiele, W. Barnes, A. Chang, E. Stocker, R. Adler, A. Hou, R. Kakar, F. Wentz, P. Ashcroft, T. Kozu, Y. Hong, K. Okamoto, T. Iguchi, H. Kuroiwa, E. Im, Z. Haddad, G. Huffman, B. Ferrier, W. Olson, E. Zipser, E. Smith, T. Wilheit, G. North, T. Krishnamurti and K. Nakamura, 2000: The status of the Tropical Rainfall Measuring Mission (TRMM) after two years in orbit. *J. Appl. Meteor.,* **39**,1965—1982.

Lau, K-M and H. Wu, 2001: Principal modes of rainfall-SST variability of the Asian summer monsoon: A reassessment of the monsoon-ENSO relationship. *J. Climate,* **14**, 2880—2895.

Li, B., M. G. Genton, and M. Sherman, 2007: A nonparametric assessment of properties of space-time covariance functions. *J. Amer. Stat. Assoc.,* **102**, 736—744.

—, —, and —, 2008: On the asymptotic joint distribution of sample space-time covariance estimators. *Bernoulli*, **14**, 228—248.

—, A. Murthi, K. P. Bowman, G. R. North, M. G. Genton and M. Sherman, 2008: Statistical tests of Taylors hypothesis: An application to precipitation fields. *J. Hydro. Meteor.,* **10**, 254–265.

Mo, K. C. and R. W. Higgins, 1998: Tropical influences on California precipitation. *J. Climate,* **11**, 412—430.

Montroy, D. L., 1997: Linear relation of central and eastern North American precipitation to tropical Pacific sea surface temperature anomalies. *J. Climate,* **10**, 541—558.

Nanjundiah, R. S., V. Vidyunmala and J. Srinivasan, 2005: On the differences in the seasonal cycle of rainfall over India in the Community Climate System Model (CCSM2) and the Community Atmosphere Model (CAM2). *Geophys. Res. Lett.,* **32**, L20720, doi:10.1029/2005GL024278.

Nicholson, S. E., 2000: The nature of rainfall variability over Africa on time scales of decades to millenia. *Glob. Planet. Change* **26**, 137—158.

North, G. R., 1987: Sampling studies for satellite estimation of rain. Preprint. 10th Conference on Probability and Statistics in the Atmospheric Sciences, Edmonton,

AB, Canada.

—, and S. Nakamoto, 1989: Formalism for comparing rain estimation designs. *J. Atmos. Ocean. Tech*, **6**, 985—992.

Poveda, G., and M. D. Zuluaga, 2005: Testing Taylor's hypothesis in Amazonian rainfall fields during the WETAMC/LBA experiment. *Adv. Water Resources*, **28**, 1230—1239.

Reynolds, R. W., and T. M. Smith, 1994: Improved global sea surface temperature analysis. *J. Climate,* **7**, 928—948.

Ropelewski, C. and M. Halpert, 1987: Global and regional scale precipitation patterns associated with the El Niño/Southern Oscillation. *Mon. Wea. Rev.,* **115**, 1606—1626.

Shin, K-S and G. R. North, 1988: Sampling error study for rainfall estimate by satellite using a stochastic model. *J. Appl. Meteorol.*, **27**, 1218—1231.

Sun, C.-H. and L. R. Thorne, 1995: Inferring spatial cloud statistics from limited field-of-view, zenith observations. *Proc. Fifth Atmos. Rad. Measure. (ARM) Science Team Meeting*, San Diego, CA. Available at http://www.arm.gov/publications/proceedings/conf05/extended_abs/sun_ch.pdf

Sylla, M. B., E. Coppola, L. Mariotti, F. Giorgi, P. M. Ruti, A. Dell'Aquila and X. Q. Bi, 2009: Multiyear simulation of the African climate using a regional climate model (RegCM3) with high resolution ERA-interim reanalysis. *Climate Dyn.*, Available at http://www.springerlink.com/content/l388325106804249/fulltext.pdf.

Taylor, G. I., 1938: The spectrum of turbulence. *Proc. Roy. Soc. London Ser. A*, **164**, 476—490.

Tracton, M. S. and E. Kalnay, 1993: Operational ensemble prediction at the National Meteorological Center: Practical aspects. Weather and Forecasting, **8**, 379—398.

Trenberth K. E., 1997: Atmospheric moisture recycling: Role of advection and local evaporation. *J. Climate,* **12**, 1368—1381.

Waymire, E., V. K. Gupta, and I. Rodriguez-Iturbe, 1984: A spectral theory of rainfall intensity at the meso-β scale, *Water Resources Research*, **20**, 1453—1465.

Zawadzki, I. I., 1973: Statistical properties of precipitation patterns, *J. App. Meteor.,* **12**, 459—472.

Zhang G. J. and N. A. McFarlane, 1995: Sensitivity of climate simulations to the parameterization of cumulus convection in the Canadian climate centre general circulation model. *Atm-ocean*, **33**, 407—446, doi 0705-5900/95/0000-0407501.25/0.

VITA

Aditya Murthi was born in New Delhi, India. He obtained his Bachelor of Engineering degree (with honors) in mechanical engineering from Amrita Institute of Technology and Science, Bharathiyar University, Coimbatore, India, in April 2001. Before joining Texas A&M University in Fall 2001, he taught at an aeronautical institute.

He received his Master of Science degree at Texas A&M University in aerospace engineering in 2004. He then joined the doctoral program in atmospheric sciences in 2006, supported by a three-year NASA Earth System Science Fellowship, and graduated with his Ph.D. in May 2010. He can be reached at the Department of Atmospheric Sciences, MS 3150, Texas A&M University, College Station, Texas 77843-3150.

The typist for this dissertation was Aditya Murthi.